VRIJE
UNIVERSITEIT
BRUSSEL

Graduation thesis submitted in partial of the requirements for the degree of Master in Physics and Astronomy

GRAZING ANGLE TEST BEAM STUDIES OF THE HYBRID-TO-MONOLITHIC MAPS PROTOTYPE

Ono Feyens

May 2025

Promotors: Prof. Dr. Michael Tytgat
Sara Ruiz Daza
Dr. Simon Spannagel

Sciences and Bioengineering Sciences

Abstract

The Tangerine group at DESY, Hamburg, investigates the potential of Monolithic Active Pixel Sensors (MAPS) manufactured in a novel 65 nm CMOS imaging process with small collection electrode design, as a candidate technology for vertex and tracking detectors in future lepton collider experiments. One of the activities undertaken to explore the technology is the characterisation of prototypes through the analysis of test beam measurements. The device under test in this thesis is the Hybrid-to-Monolithic (H2M) chip. The investigated property is the active thickness of the sensor. This is done via the so-called grazing angle method, in which information about the charge collection as a function of depth inside the sensor is generated through the use of ionizing particles impinging the sensor under shallow angles. This concept is practically realized through the conduction of test beam measurements, and a two-step data analysis procedure, in which first the data were organized and then charge collection profiles were constructed, displaying the amount of collected charge as a function of depth inside the sensor. The total active thickness is found to be approximately 13 µm, of which $\sim$ 2 µm corresponds to an incomplete collection close to the sensor surface, followed by $\sim$ 6 µm of uniform collection and $\sim$ 5 µm of exponentially decreasing collected amount of charge. The impact of several chip parameters on the active thickness is investigated. Backside thinning to 25 µm, impinging the sensor from sensor surface or backside, varying hit detection threshold, and changes in applied sensor bias voltage are all found to not significantly influence the active thickness of the sensor. The results furthermore validated the function of the threshold and ToT calibration procedure to correct for non-linear electronics responses.

Disclaimer

Large language models (LLMs), such as ChatGPT of OpenAI, were used to assist in improving the clarity and structure of the written text, as well as to support the development and refinement of analysis code used to construct most of the plots represented in the thesis. All final content, interpretations, and conclusions remain the responsibility of the author.

Contents

1. Introduction

Throughout human history, there has always been a quest to comprehend the fundamental components of the Universe and the laws that govern its behaviour. This human curiosity has driven the development of numerous theories to explain experimental observations and inspired experiments to validate theoretical predictions. Since the late 1800s, this interplay between theory and experiment has been present in particle physics, beginning with what is considered the birth of the field of particle physics: J.J. Thomson's discovery of the electron in 1897 [1]. Over the following century, an ever-growing number of particles were predicted and discovered. Groundbreaking insights into the fundamental forces governing the interactions between the particles were made. Finally, in 2012, the Higgs boson was discovered at the Large Hadron Collider (LHC) [2] by the ATLAS [3] and CMS [4] collaborations at the European Organization for Nuclear Research (CERN) [5]. With all these discoveries came a search for structure, which was established by a theoretical framework describing all fundamental particles and forces (except gravity) that make up and govern the known matter in the Universe: the Standard Model (SM) of particle physics. Although the SM has demonstrated remarkable success, it leaves several fundamental questions unanswered. These open questions drive the development of high-energy particle physics experiments, particularly particle colliders. To enable precise measurements, colliders are equipped with complex experiments composed of multiple detector systems, some of which rely on silicon-based sensors. The research presented in this thesis contributes to the R&D of silicon sensors for use in future collider experiments succeeding the LHC, which is currently the primary operational accelerator.

Before delving into the details of the conducted research, Chapter 2 provides a brief overview of the SM as well as the structure and requirements of experiments at future colliders. Chapter 3 then outlines the operating principles of semiconductor particle detectors. The specific device studied in this work is introduced in Chapter 4. The primary objective of this research is to determine the sensor's active thickness—that is, the region in which incident particles are effectively detected. To achieve this, the so-called grazing angle method is employed. The objective and approach are presented in Chapter 5. Chapter 6 describes the experimental setup used to collect the necessary data, which is summarized in Chapter 7. The data analysis strategy used to extract information about the sensor's active thickness is detailed in Chapter 8, with the results presented and discussed in Chapter 9.

2. Particle physics at collider experiments

This chapter aims to outline the broader context in which the research presented in this thesis was conducted. It offers an overview of our current understanding of particle physics, as described by the Standard Model, and highlights the questions that remain unanswered by this framework. It also examines the role of future colliders in advancing particle physics and outlines the general design and requirements of experiments at these colliders.

2.1 The Standard Model of particle physics

2.1.1 Current understanding

The Standard Model of particle physics provides a unified picture of the fundamental constituents of the Universe, called fermions, and the interactions between them, the forces, which are themselves described by the exchange of particles called bosons [6].

All known matter in the Universe is made up of twelve fundamental particles called fermions, which are grouped into three generations, each distinguished by increasing mass. Each of the twelve fermions has a corresponding antiparticle with identical mass but opposite charge. Substance made from these antiparticles is called antimatter. The particles interact with one another via the four fundamental forces: gravity, electromagnetism, the strong force, and the weak force. Each fundamental force, except for gravity, is described by the exchange of a force carrier particle, also called a gauge boson. An overview of the elementary particles of the Standard Model is shown in Figure 2.1.

2.1.2 Unanswered questions and anomalies

The Standard Model of particle physics is one of the most successful scientific frameworks, offering a remarkably accurate and extensively tested description of the fundamental particles and forces that shape the Universe, yet it leaves critical theoretical and experimental questions unanswered [8]. A few example of these open questions are discussed in this section.

Among the most compelling of the mysteries is the nature of dark matter. Numerous experiments have provided evidence of the existence of a type of matter that does only interact gravitationally with the matter described by the SM. However, no SM particle meets the requirements to be such a dark matter candidate. The SM also does not provide a candidate for whatever is responsible for the observed accelerated expansion of the Universe, often attributed to dark energy. Another unexplained observation is the imbalance between the amount of matter and antimatter, known as the matter-antimatter asymmetry. As discussed, the matter

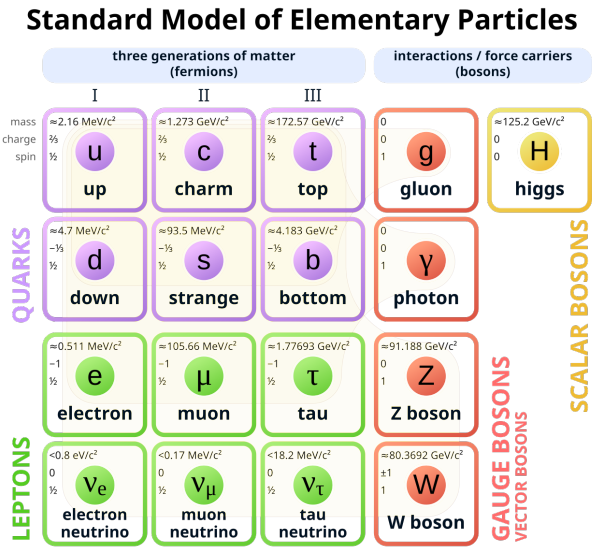

Figure 2.1: Elementary particles of the Standard Model of particle physics. Figure from [7]

particles are divided into three generations with increasing mass, however, the reason for this separation and the wide observed range of masses, is not provided within the SM. Similarly, no explanation is given for the existence and hierarchy of the neutrino masses.

Several "anomalies", i.e. deviations from the SM predictions, are observed in particle physics experiments and hint towards new physics [9]. An example of such an anomaly is the W mass, measured at the Tevatron [10], which is inconsistent with the SM prediction and measurements performed by other experiments.

However experimentally confirmed in 2012, the Higgs boson also requests some further experimental investigation [11]. For example, it remains unclear whether it is an elementary or composite particle, and its self-coupling has yet to be experimentally confirmed.

2.2 Future colliders in particle physics

The existence of open problems within the SM, of which some are listed in the previous section, indicate the need for further experimental investigation in the field of particle physics. The experimental technique which has been proven successful by multiple discoveries in the field for more than a century, are particle colliders.

2.2.1 Particle colliders

A particle accelerator is a device that increases the kinetic energy of particles, accelerating them to near-light speeds. The accelerated particles, also called particle beams, can be brought into collision producing individual interactions referred to as events [6]. Two main types of accelerators are distinguished: particle colliders, where two particle beams are brought into head-on

collisions, and fixed-target experiments, where a single beam strikes a stationary target. In the introduced collisions, the collision energy is transformed into matter in the form of new particles, as described by Einstein's mass-energy equivalence formula $E = mc^2$ [12]. Thus, in order to produce massive particles such as the $W^{\pm}$, Z or Higgs boson, a high collision energy is required. More precisely, from a kinematic point of view, in the centre-of-mass frame, where the total momentum of all particles included in the collision is zero, the centre-of-mass energy $\sqrt{s}$ must be bigger than the sum of the masses of all particles emerging from the collision. The centre-of-mass energy $\sqrt{s}$ is defined as the square root of the total energy and momentum of the two colliding particles, denoted as s. Due to the asymmetric geometry in a fixed-target experiment, the collision products will always be produced with a significant amount of kinetic energy, due to momentum conservation. Effectively meaning that part of the initial energy is not available as centre-of-mass energy for the production of new particles. As the collisions in collider experiments take place in the centre-of-mass frame, the available amount of energy for the creation of new particles is equal to the sum of the energies of the colliding particles; providing these machines with the ability to reach much higher centre-of-mass energies, and thus create particles with a higher mass. This is why such collider designs are commonly employed. The centre-of-mass energy is one of the most important parameters of a particle accelerator as it determines the types of particles that can be investigated. Another key parameter is the luminosity $\mathcal{L}$, which determines the event rate. Particle colliders with a high luminosity enable the study of rare processes by increasing the probability of observing them.

Many different species of particles can be brought into collision in colliders: leptons (electrons, positrons, muons (in principle) ...), hadrons (protons, antiprotons, ...), ions, nuclei, ... Depending on the colliding particles, different physics programmes are enabled [6, 8, 11] as the collision environments created by the different particles varies. Colliding elementary particles that do not interact through the strong force, such as electrons and positrons, comes with the advantage of certainty about the initially interacting particles and a clean collision environment. This makes them especially suited for precision measurements in which one aims to determine the physical quantities with a high accuracy and minimal uncertainty. On the other hand, for composite particles of which the constituents (called partons) do interact via the strong force, such as protons, an assumption has to be made on which of the partons actually collided and with which fraction of the proton energy. Another disadvantage of colliding these particles is that the collisions come with a significantly higher background, i.e. signals mimicking the signature of the process of interest but actually being caused by other processes, which is mainly due to the nature of the strong interactions. When a circular accelerator design is employed, hadron colliders have the advantage of being able to reach higher energies ($> 350\,\text{GeV}$), since they are less affected by synchrotron radiation, occurring when the trajectory of charged particles is bent [6].

2.2.2 Future particle colliders

Guided by the success from the past, the idea now is to face the current challenges in particle physics by means of experimental measurements conducted at a collider site. Currently, the most powerful collider is the LHC [2] at CERN [5]. However, so far no indications of beyond the Standard Model (BSM) physics were observed. In the upcoming years, the LHC will be upgraded to the High-Luminosity Large Hadron Collider (HL-LHC) [13], characterized by an

instantaneous luminosity 5 to 7.5 times higher than the LHC's design value and an integrated luminosity of a factor of 10 beyond the LHC's design value. This will enable the collection of increased amount of data, making it possible to extend the measurements providing confirmation of the predictions of the SM to great precision as well as to measure Higgs boson properties in more detail [11]. However, tackling the problems denoted in Section 2.1.2 seem to require a successor of the LHC.

The potential of colliders as tools for advancing particle physics is acknowledged in the European Strategy for Particle Physics (ESPP) [14]. The Stategy articulates the ambitions of the particle physics community from a European perspective, situated within a global framework. In the version updated in 2020, the importance of extending the current boundaries of knowledge is underscored, and colliders are identified as central to this objective. It is stated that

'An electron-positron Higgs factory is the highest-priority next collider. For the longer term, the European particle physics community has the ambition to operate a proton-proton collider at the highest achievable energy.'.

A Higgs factory is essentially a collider which is optimized to produce Higgs bosons at a high rate. The physics programme that will be enabled by these future colliders, focuses on the required investigations. The idea is to use the lepton collider for multiple precision studies, among which of the $W^{\pm}$, Z and Higgs bosons. Whereas the succeeding hadron collider will extend the search for new phenomena possibly related to the open questions within the SM. As the exact energy scale at which these phenomena will appear is not known, it seems like the field may be shifting from being theory-driven to being more experimentally driven [8]. The separation in the physics programmes in terms of precision / BSM probe of the future colliders is in fact not that clear. For instance, a deviation observed in a high-precision measurement of a SM process could indicate the presence of BSM physics. While in the context of BSM searches, deviations from expected background predictions may reveal inconsistencies in the predictions from SM backgrounds [8].

However the LHC is still expected to deliver many valuable physics results, preparations for the its successors are already fully ongoing as the time required to design and construct large colliders can range from a decade to a half-century. Several designs for both the electron-positron and hadron collider have already been proposed. For the electron-positron collider, which is of interest in this thesis, there are currently four well-established designs. The Compact Linear Collider CLIC [15] and Future Circular Lepton Collider FCC-ee [16] are two designs proposed by CERN. The Circular Electron Positron Collider CEPC [17] is a project proposed by China and the International Linear Collider ILC [18] would be located in Japan.

2.3 Experiments at future colliders

2.3.1 Structure overview

In order to study the physics processes at particle accelerators, sophisticated detectors, known as collider experiments, are placed at the interaction points. Their purpose is to detect and

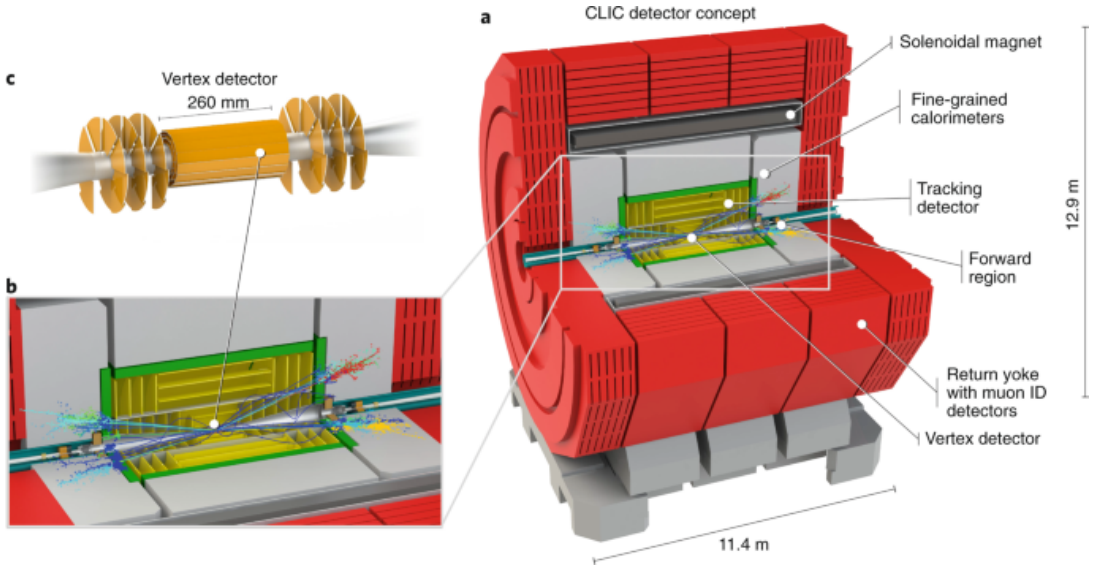

Figure 2.2: The CLIC detector concept (a), its tracking system (b) and vertex detector (c). Figure from [19].

measure the properties of the observable[1] particles emerging from the high-energy collisions, in order to reconstruct the primary particles produced in the interactions. For this purpose the collider experiment is divided into multiple layers of detectors, each optimized to detect specific types of particles and to measure particular properties. In currently operating particle colliders, these subdetector layers are arranged in an onion-like structure around the beam axis and the interaction point. Future collider experiments will likely follow this well-established onion-like structure. Figure 2.2 presents the proposed design of the experiment at the CLIC collider, illustrating the characteristic onion-like detector structure.

The sequence of subdetector layers traversed by the collision products in a collider experiment is carefully optimized to maximize the amount and quality of information that can be extracted [6]. From the innermost to the outermost layers, a typical collider experiment comprises a tracking system devoted to the reconstruction of trajectories of charged particles, followed by an electromagnetic calorimeter for the detection of electrons and photons and a hadron calorimeter for the detection and measurement of the energy of hadrons. Finally, the outer layer of the experiment is dedicated to the detection of high-energy muons [6]. This sequence can also be observed in Figure 2.2. The identification of collision products is achieved by combining data from all parts of the detector system. While the design of collider experiments can vary and often includes additional components such as RICH or Time-of-Flight detectors, this section does not aim to describe the full detector system. Rather, it focuses on placing the tracking system — the subject of this thesis — in context. The discussion that follows will therefore concentrate solely on this component.

The operation of particle detectors relies on the interactions between incoming particles and

[1] Of all produced particles, only the stable (e.g. electrons) and relatively long-lived (e.g. muons) particles are observable [6].

the detector material [20]. Relativistic charged particles traversing a detector medium primarily interact electromagnetically with atomic electrons, leading to ionisation [6]. This ionisation can be detected and forms the fundamental principle behind tracking detectors based on semiconductor technology, as described in more detail in Chapter 3. To reconstruct particle trajectories, the tracking system consists of multiple layers of silicon sensors. As particles pass through these layers, they produce signals, referred to as hits, in each layer. By connecting these hits, the trajectory of the particle can be reconstructed [6]. To measure the particle's momentum, the tracking system is typically enclosed within a large magnet that generates a (uniform) magnetic field parallel to the beam direction. As particles emerge from collisions, their paths are curved by the Lorentz force. By analysing the curvature of these trajectories, the momentum of the particles can be determined. For optimal momentum resolution, it is crucial to minimize the energy loss caused by ionising interactions. This requires reducing the amount of material the particles pass through. Consequently, the tracking system is located in the innermost region of the detector. Minimizing the material budget is one of the key objectives of detector design and construction.

The tracking system can be divided into two main components: the vertex detector and the tracking detector. The vertex detector, positioned closest to the interaction point, is designed to determine particle trajectories with such precision that the exact collision location, referred to as the vertex, can be identified. When unstable yet relatively long-lived particles are produced in collisions, their decays give rise to secondary vertices — the points where these particles decay — which can also be reconstructed by the vertex detector. This principle is for example used for the identification of b-quarks [6]. These b-quark hadrons are relatively long-lived and will be able to travel on average a few millimetres away from the interaction point - the primary vertex - before they decay in the secondary vertex. This experimental signature can be reconstructed by means of a high-precision vertex detector. The tracking detector, on the other hand, aims to reconstruct particle momenta by measuring the curvature of their trajectories. This requires a larger detector volume but allows for a small spatial resolution. The proposed design of the complete tracking system (b), along with a zoomed view of the vertex detector (c) for the CLIC collider, is shown in Figure 2.2.

2.3.2 Requirements

In the ESPP, the need for a global detector R&D roadmap is emphasized. This need has been addressed in 2021 by the Detector R&D Roadmap developed by the European Committee for Future Accelerators (ECFA) [21]. This roadmap outlines the technological requirements to achieve the science programme specified in the ESPP. The section on solid-state sensors presents an overview of their performance and design targets for use as vertex and tracking detectors in future collider experiments. Table 2.1 summarizes key requirements for silicon sensors at future lepton colliders [21]. The quoted values are those estimated for the CLIC collider design. The design of the CLIC vertex detector and tracking system is driven by the demands of high-precision measurement [22]. Such measurements rely on both the accurate reconstruction of particle momenta and the ability to clearly distinguish signal events from background. As discussed in the previous section, the vertex detector plays a key role in identifying the flavour of quarks—particularly in tagging heavy-flavour quarks such as b-quarks—through the reconstruction of secondary vertices. This capability is essential for suppressing background processes

Table 2.1: Overview of performance and design targets of vertex and tracking detectors in future lepton collider experiments. The quoted values are required for CLIC. Adapted from [21, 23].

Detector type	Vertex	Tracking
Material budget X/X_0 [%/layer]	$\simeq 0.1$	$\simeq 8$
Position resolution [µm]	$\lesssim 3$	$\simeq 7$
Time resolution [ns]	~ 1	~ 0.1

and isolating events of physical interest [6].

The research presented in this thesis is conducted in the context of the investigation of novel silicon detector technologies to meet these requirements. More precisely, the Hybrid-to-Monolithic (H2M) chip will be investigated in the context of the Tangerine project at Deutsches Elektronen-Synchrotron (DESY) focusing on Monolithic Active Pixel Sensors (MAPS) manufactured in a 65 nm Complementary Metal-Oxide-Semiconductor (CMOS) Imaging Technology with small collection electrode design. Before delving into the details of this project and the device under test (DUT), a more general description of semiconductor particle detectors is provided in the next chapter.

3. Semiconductor particle detectors

The operation of particle detectors relies on the interactions between incoming particles and the detector material. The first section of this chapter focusses on the interaction mechanisms relevant to this thesis. The second section focusses on the detector principle of interest in this thesis: semiconductor particle detectors, with a special focus on silicon sensors.

3.1 Particle interactions with matter

When particles traverse matter, they interact with the material and lose energy [24]. Particle detectors exploit these interaction mechanisms to detect and measure various particle properties, as mentioned in the previous chapter.

In this work, charge collection in a 50 µm thin silicon sensor is studied using electron beams with energies around 5 GeV. The primary energy loss mechanisms in the detector material are ionisation, excitation, and bremsstrahlung. Multiple Coulomb scattering may also occur, but since it deposits relatively little energy, it does not contribute to particle detection—though it remains relevant due to its deflective effect on particle trajectories.

3.1.1 Ionisation and excitation

Charged particles can interact with the atomic shell of the atoms of the detector material [24]. Both ionisation, in which sufficient energy is transferred to release an electron from the atom, and excitation, in which an electron is brought to a higher energy level without being liberated from the atom, can take place. The mean amount of energy a particle loses per path length is described by the Bethe-Bloch formula. If this measure is plotted as a function of the energy of the traversing particle, a region can be identified where the particle loses a minimum amount of energy. Particles in the corresponding kinematic range are called Minimum-Ionizing Particles (MIP).

The total energy deposited as a particle traverses a certain distance in the detector medium arises from numerous subsequent ionisation and excitation interactions, each contributing a portion of the total energy. The amount of energy transferred in each of these interactions is subject to statistical fluctuations. In many interactions, a small amount of energy is transferred. However, in some events, a large amount of energy is lost. The events in which a higher amount of energy is lost, correspond to rather rarely occurring hard collisions in which a significant amount of energy is transferred to one single electron, which then possess sufficient kinetic energy to further ionize the material [24, 20]. These electrons, responsible for additional or sec-

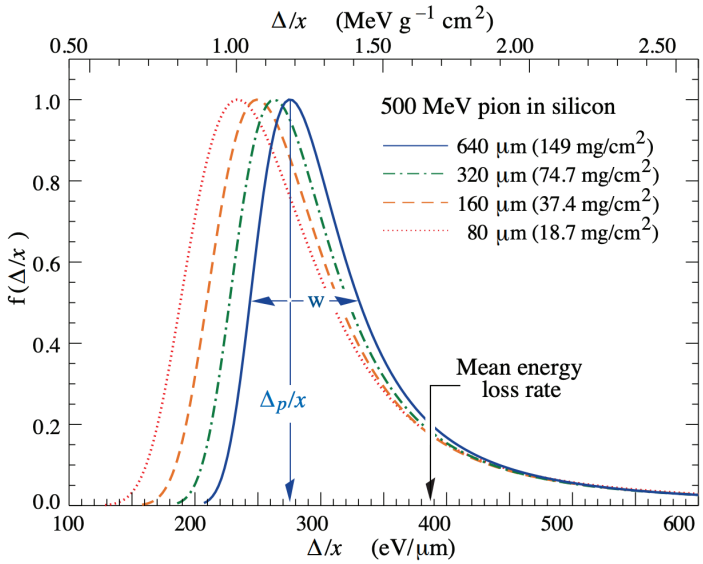

Figure 3.1: Landau distributions, normalized to the traversed thickness, from [25].

ondary ionization, are referred to as δ-electrons. These energy transfer fluctuations in individual collisions along the particle's path through the medium lead to an asymmetric distribution, exhibiting a Gaussian part corresponding to the many ionisation processes with small energy loss and a tail to large energy loss values owing to the δ-electrons. The function describing this distribution is the Landau distribution. Examples of Landau distributions, normalized to the traversed thickness by the particle, are shown in Figure 3.1. Notable is the difference between the Most Probable Value (MPV), being the maximum of the distribution, and the mean energy loss rate. Due to the presence of δ-electron events, the average is shifted to higher energy values with respect to the MPV. The different distributions shown in Figure 3.1 are corresponding to different traversed thicknesses by the particle. Remarkable is the dependence of the MPV on the traversed total thickness, even after normalisation to the total traversed thickness.

In fact, however, the distribution measured by a particle detector is not exactly a Landau distribution. Namely, the electronics and readout system of the detector introduce an additional smearing. Usually, these detector effect follow a Gaussian distribution [24]. Therefore, at the end, the measured distribution is a convolution of a Landau distribution, which models the statistical fluctuations around the mean deposited energy, and a Gaussian distribution, which accounts for the smearing from the detector response. As the Landau component is the one related to the underlying particle interactions and deposited energy, the MPV of the Landau distribution is often used to describe the energy deposited in the detector.

3.1.2 Bremsstrahlung

If the energy of the traversing charged particles exceed a certain threshold energy, known as the critical energy, the most dominant mechanism by which they lose energy in the material shifts from ionisation and excitation to bremsstrahlung. In bremsstrahlung interactions the charged particles lose energy by means of photon radiation in the Coulomb fields of the atomic nuclei

[24]. As the energy loss is inversely proportional to the squared mass of the traversing particle, mainly lower mass particles, such as electrons, are affected by this mechanism.

The critical energy in silicon is 40.2 MeV [24], making bremsstrahlung the dominant energy loss mechanism for an electron beam of approximately 5 GeV. Due to ionisation about 387 eV μm^{-1} is deposited in silicon [24], resulting in roughly 19 keV of deposited energy for a 50 µm thick sensor. In contrast, the energy lost through bremsstrahlung in this same sensor is around 2.7 MeV, determined from the radiation length X_0 of 9.36 cm [24] over which the particle loses about 63 % of its initial amount of energy. Despite this, the generated energy loss distribution in the detector follows a Landau shape, characteristic of ionisation. This is because bremsstrahlung losses primarily produce photons, which, in thin silicon sensors, are likely to escape without depositing their energy in the detector material—thus not contributing to the detected signal. In contrast, ionisation deposits energy locally within the detector, making it detectable.

3.1.3 Multiple Coulomb scattering

A charged particle passing through a material, undergoes in general multiple scattering processes under the influence of the Coulomb fields of the material's atomic nuclei [24]. These subsequent scattering processes are referred to as multiple Coulomb scattering. If the scattered particle is light compared to the mass of the nucleus, the particle will be deflected with only a small energy transfer to the nucleus. Multiple Coulomb scattering interactions thus result in a change in the particle's trajectory without a deposition of a significant amount of energy in the material. The scattering angle relative to the particle's original direction follows an approximately Gaussian distribution, with a standard deviation proportional to the material budget, x/X_0, where x is the thickness of the detector material and X_0 is the radiation length of the medium. This underscores the importance of minimizing the material budget in silicon sensors used in tracking and vertex detectors. A thicker sensor increases the material budget, leading to a greater spread in the scattering angle and, consequently, a higher uncertainty in track reconstruction [24].

3.2 Semiconductor particle detectors

The sensitive material of the detectors investigated in this thesis is silicon, a so-called semiconductor. This section focuses on semiconductor properties and how they are utilized as particle detectors, with a specific focus on silicon sensors.

3.2.1 Semiconductors

In semiconductors, which are solid state materials, the atoms are closely packed in a periodic crystal lattice [24, 20]. This periodic atomic arrangement establishes allowed energy bands, in contrast to discrete energy levels in isolated atoms, for the electrons. At temperature $T = 0\,\mathrm{K}$, the valance band (VB) is completely occupied with outer shell electrons bound to specific atomic sites. As no free charge carriers are present, current cannot flow, and the material is non-conductive. The highest occupied energy level at 0 K marks the so-called Fermi level E_f. At $T > 0\,\mathrm{K}$, some electrons from the VB are thermally excited into the higher-energy conduction band (CB). This is possible in semiconductors, as they exhibit a relatively small band gap E_g, which is the difference in energy between the CB and the VB (e.g. 1.12 eV in silicon),

which can be overcome by thermal energy. The thermal excitations induce electrons in the now partially filled CB, and create unoccupied states in the VB. These unoccupied states in the VB are referred to as (virtual) charge carriers: the positively charged holes. The transitions of electrons within the CB and holes within the VB between available energy levels is responsible for the conductivity of the material.

Two types of semiconductors are distinguished: pure or intrinsic and doped or extrinsic semiconductor materials. The first one refers to semiconducting materials in which no "impurities" are present. Electrons only entered the VB through thermal excitation, which means that under thermal equilibrium, the concentration of electrons and holes in the CB and VB, respectively, is equivalent. Thus in an intrinsic semiconductor, both free electrons and holes contribute to current flow. The Fermi level is located in the middle of the band gap. In an extrinsic semiconductor, "impurities" or "dopants" are present in the material. These dopants add extra allowed energy levels for either the electrons or holes, causing extra electrons or holes to participate in the conduction process. There are two types of doped semiconductors: n-type and p-type. An n-type semiconductor is doped with donor impurities (such as phosphorus for silicon), adding extra electrons in the CB. These electrons, which have become the majority charge carriers, is responsible for conductivity in the material. The Fermi level is shifted closer to the CB. Something similar applies to the p-type semiconductors, only now the positively charged holes in the VB is in the majority due to the presence of acceptor impurities (such as boron for silicon). In a p-type semiconductor the holes in the VB are responsible for the conduction of electrical current in the material and the Fermi level is shifted closer to the VB.
The impurity concentration in doped semiconductors is often indicated using notation such as n^+ or p^+ for heavily doped (high-concentration) regions, and n^- or p^- for lightly doped (low-concentration) regions [20].

3.2.2 Pn-junction

A pn-junction is formed when p- and n-type semiconductor materials are brought in contact [24]. The holes from the p-side diffuse toward the n-side, where they recombine with electrons, leaving behind immobile, negatively charged acceptor ions on the p-side. In the opposite direction, the electrons from the n-side diffuse towards the p-side where they recombine with the holes, leaving behind immobile positively charged donor ions on the n-side. The recombinations, taking place at the boundary of the two semiconductor types, form a region without any free charge carriers (electrons or holes), the so-called depletion region. The accumulated space charge formed by ionized dopants which are left behind in the depletion region form an electric field, counteracting the diffusion effect. This intrinsic potential difference is called the built-in potential. It is this depletion region which acts as the detector medium in semiconductor detectors. Namely, the electron-hole pairs generated by impinging charged particles or absorbed photons in this region, are swept out of the depletion region by the intrinsic electric field. The motion of the charge carriers constitutes the electrical signal marking the detection of a particle [20].

The extend of the depletion region can be modified by applying an external voltage [24]. If the external voltage is applied in a reverse way (i.e. connecting the negative electrode of the voltage source to the p-side of the pn-junction and the positive electrode to the n-side) the width of the depletion region is increased as now both the holes on the p-side and the electrons on the n-side

are pulled away from the boundary region in the pn-junction. Reverse biasing a pn-junction thus increases the active volume of the semiconductor detector. The resulting stronger electric field accelerates the generated electron-hole pairs more efficiently, reducing the time needed for the carriers to be collected at the electrodes and lowering the probability of recombination or trapping, which leads to increased charge collection.

3.2.3 Movement and collection of charge carriers

There are two possible charge carrier transport mechanisms: *drift* and *diffusion*. Under the presence of an electric field in the semiconductor material, the charge carriers follow a drift movement dictated by the direction and with a velocity proportional to the strength of the electric field. In the absence of an electric field, or when only a weak one is present, diffusion becomes the dominant transport mechanism for charge carriers. This process results from thermal motion and occurs due to a carrier concentration gradient, leading to random, uncoordinated movement. The currents associated to these movements are given by [24]

$$\vec{j}_{\text{drift}} = \sigma \vec{E},$$

and

$$\vec{j}_{n,diff} = -eD_n \vec{\nabla} n, \tag{3.1}$$

with σ the conductivity of the material, $\vec{E}$ the electric field, e the elementary charge, n the negative charge carrier density (electron density) and D_n is the diffusion coefficient for electrons. Equation (3.1) is explicitly written down for electrons; simply changing the n to a p provides the alternative formula for holes.

An expression for the change in charge carrier density in a certain volume in the sensor, can be determined by exploiting the continuity equation and the formulas for the carrier currents introduced by the movements of the charges [24]. In the case of an environment in which diffusion is the dominant carrier transport mechanism and no new charges are being generated, the expression can explicitly be written down in one-dimension for electrons as [26]

$$\frac{\partial n}{\partial t} = -\frac{n}{\tau_n} + D_n \frac{\partial^2 n}{\partial x^2}, \tag{3.2}$$

where the first term on the right hand side accounts for recombination losses and the second term describes the diffusion. τ_n is the carrier lifetime of electrons, defined as [24]

$$\tau_n = \frac{L_n^2}{D_n}, \tag{3.3}$$

where L_n is the average length an electron can travel before it undergoes recombination, also referred to as the diffusion length.

3.2.4 Monolithic Active Pixel Sensors (MAPS)

Pixel sensors are created by segmenting a pn-junction in two directions and connecting electrodes to each of the formed pixels separately. As a particle deposits energy in the detector

volume (silicon), it creates electron-hole pairs, which are separated by the electric field (enhanced by applying a reverse bias voltage). The movement of the charge carriers induces a signal in the readout electronics [24].

In Monolithic Active Pixel Sensors (MAPS) both the particle sensing part (sensor) and the CMOS electronics circuitry are merged into one single volume. Compared to hybrid pixel detectors, where the sensor and electronics parts are separately manufactured and combined at the end by means of bump-bonds, the MAPS design enables lower material budget, and reduced production cost as the complex and expensive bump-bond procedure is omitted [24]. A more detailed description of the sensor layout of a MAPS is provided in Chapter 4.

MAPS have seen significant advancements in recent years. One place where this technology is currently in use is the inner tracker of the ALICE experiment at the LHC. During the long shutdown of the LHC in 2019-2020 the Inner Tracking System (ITS) of ALICE was upgraded to a system consisting of seven concentric layers of MAPS with the ALPIDE chip design, covering in total an area of $10\,\mathrm{m}^2$ [27]. These ALPIDE detectors are also being used as telescope planes in test beam setups, for example at the DESY II Test Beam Facility [28], as will be discussed in Chapter 6.

3.2.5 65 nm CMOS Imaging Technology

The DUT in this thesis is manufactured in a novel 65 nm CMOS Imaging Technology, to which the high-energy physics community only recently got access [29]. This technology allows for a higher in-pixel logic density compared to previously used processes which are characterized by a higher feature size. This makes it possible to achieve the same level of logic complexity in a reduced amount of space, enabling the reduction of pixel pitch, defined as the distance between the centres of two adjacent pixels in the matrix. Using this technology, the in-pixel functionality can also be increased. The technology process has been previously explored in prototypes such as the APTS [30] and DPTS [31].

4. The Tangerine project and Hybrid-to-Monolithic (H2M) chip

4.1 The Tangerine project

The work presented in this thesis is carried out within the research framework of the Tangerine project (Towards Next Generation Silicon Detectors) at DESY in Hamburg [29]. As the name suggests, the aim of this project is to develop the next generation of silicon sensors fabricated in novel technologies. Part of the focus goes to the investigation of MAPS sensors manufactured in a novel 65 nm CMOS Imaging Technology with a small collection electrode design as a candidate to meet the requirements of a vertex and tracking detector at future lepton collider experiments.

To fully explore the potential of the technology, all aspects of sensor R&D are being addressed in the project [29]. The electronics and sensor designs are investigated through simulations and prototype characterisations, while technology demonstrators are characterized using both laboratory setups and test beam measurements. This thesis focusses on the latter. The demonstrator that is being investigated is the Hybrid-to-Monolithic (H2M) chip.

4.2 Hybrid-to-Monolithic (H2M) chip

H2M is a monolithic pixel sensor chip manufactured in a modified 65 nm CMOS Imaging Technology [32]. The chip contains a pixel matrix of 64 $\times$ 16 squared pixels with a pixel pitch of 35 µm. The total active area of the chip is approximately 1.25 mm^2. Each pixel is equipped are a collection electrode, analog front-end and digital logic.

4.2.1 Sensor design

Figure 4.1 shows a cross sectional illustration of one H2M pixel. The full CMOS circuitry (denoted in pink and green at the top) and active sensor volume (denoted in blue) are merged into one silicon volume, characteristic for MAPS. Charge carriers are collected in the small n-well collection electrode. The use of a small collection electrode design increases the signal-to-noise ratio which results in a lower power consumption in the analog front-end compared to large collection electrode designs, as now the needed signal amplification is reduced. To shield the CMOS electronics, consisting of both NMOS and PMOS transistors embedded in their corresponding p- and n-wells, from the sensor volume and ensure that charge is only collected in the n-well provided for this purpose, the electronics circuit is embedded in a deep p-well [33].

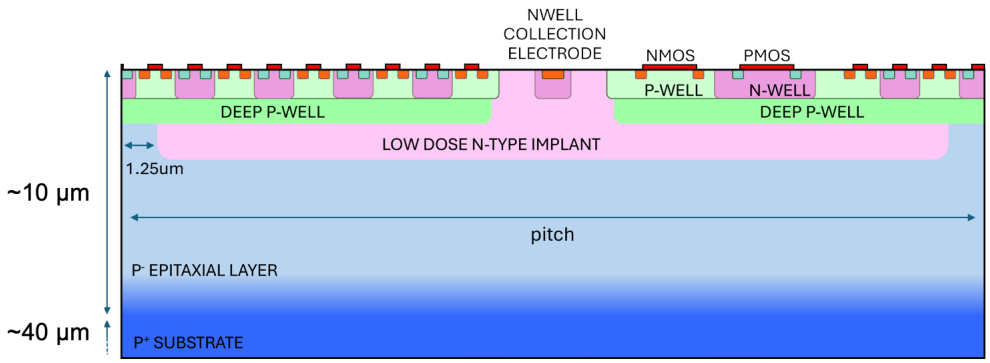

Figure 4.1: Cross sectional illustration of H2M, modified from [34].

The sensor consists of a p^+ substrate on which a p^- epitaxial layer is grown. The epi-layer is chemically purer and characterized by a higher resistivity than the substrate, allowing generated charge carriers to be detected more efficiently [24]. The sensor layout of H2M is a so-called *modified with gap* layout, due to the presence of a low dose n-type implant with gap. This modified layout improves the sensor's performance. First of all, the presence of the implant deep inside the sensor, shifts the pn-junction deeper in the sensor which allows the creation of a larger depletion region. Secondly, the gap in the deep implant increases the lateral electric field at the pixel edge, enhancing the amount of charge collected in one pixel and therefore the signal-to-noise ratio [32]. The sensor is reverse biased by applying a sensor bias voltage to the deep p-wells and substrate. The total thickness of the chip is 50 µm of which about 10 µm is the epi-layer.

4.2.2 The on-pixel analog front-end and digital logic

In the analog front-end the induced signal in the n-well collection electrode is amplified by means of a processor with a Charge-Sensitive Amplifier (CSA) which features a gain stage with a Krummenacher type feedback network which controls the rate at which the signal returns to baseline [35]. The amplified signal is provided to a comparator with a globally provided threshold voltage, set by an 8-bit DAC in the periphery. In the in-pixel comparator, the incoming signal is compared to the set threshold value. Signals that exceed the threshold value are identified as hits; therefore, the comparator threshold is also referred to as the hit detection threshold.

The digital logic, based on an 8-bit counter per pixel, is responsible for the storage of the hit information. Which information is stored, depends on the acquisition mode in which the chip is operated. There are four possible acquisition modes, of which only one can be employed at a time [36]:

- *Time-over-Threshold (ToT)* in which the amount of time the signal exceeds the hit detection threshold is measured, which is proportional to the amount of collected charge, as can be seen in Figure 4.2;
- *Time-of-Arrival (ToA)* identifying the moment the signal crosses the hit detection threshold for the first time;

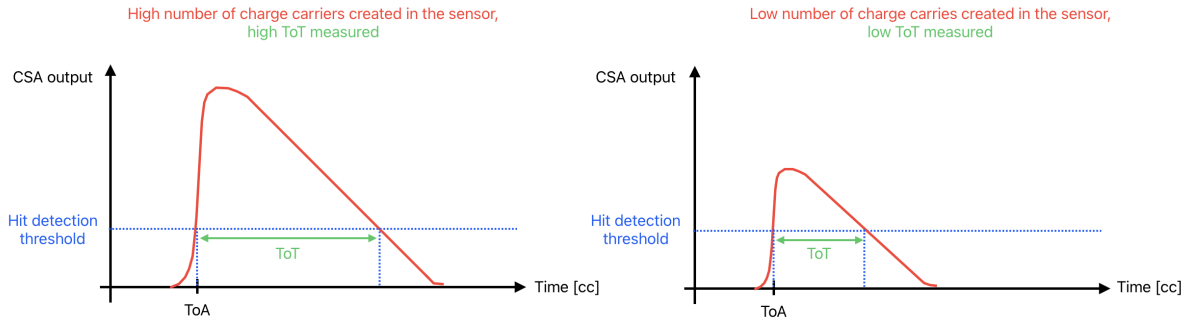

Figure 4.2: CSA output as a function of time in the readout electronics for an event in which a high (left) and low (right) number of charge carriers were generated in the sensor, illustrating how the ToT value is proportional to the amount of created charge.

- *Photon counting* in which the number of times the signal exceeds the hit detection threshold value is counted;
- *Triggered* providing a binary output identifying whether a hit occurred in the DUT within a defined time window following a hit in the trigger plane.

All data analysed in this thesis are recorded in ToT mode. The ToT information is given in clock cycles (cc), where one cc unit corresponds to 10 ns. The integration time of the readout circuit depends on the readout mode. For ToT this is approximately 10 ms. More technical details on the chip are provided in the H2M reference manual [36].

5. Research objective and approach

This chapter outlines the objective of the thesis project, explaining both its significance and the approach that will be taken to achieve it. It justifies the choices made in the experimental setup and the types of data collected, which will be discussed in the following chapters.

5.1 Research objective

As this thesis is conducted as part of the Tangerine project, its general objective is to contribute to the characterization of one of the prototypes under investigation: the H2M chip. This characterization involves systematic measurements and analysis of the chips performance, properties and behaviour under certain conditions. This knowledge will shape future decisions on silicon detector designs and more generally informs further developments in the Tangerine project and the international community working towards future lepton collider experiments.

This thesis investigates a specific property of H2M: the charge collection as a function of depth within the sensor, also referred to as the charge collection profile. From this information it is possible to determine the active thickness of the sensor, i.e. the thickness of the silicon layer from which charge is collected. The active thickness of H2M is reported to be approximately 10 µm, though the exact value remains unknown [32].
In general, the more thoroughly the prototypes are characterized, the clearer the insights into potential improvements for the final chip design. Insights into the charge collection profile and active thickness are especially important for providing feedback to chip designers and those involved in simulations.
First of all, if the thickness of the active region is known and one makes an assumption about the amount of charge generated per µm traversed in the sensor, one can in principle have an idea about the expected amount of collected charge in the sensor [20]. This information is valuable for the chip designers since it gives an idea about the way in which the front-end parameters in the final chip design should be tuned with respect to their settings in the prototype. A concrete example of one of these parameters is the hit detection threshold voltage, which is set by an 8-bit DAC in the periphery. Having this rather large dynamic range[1] for the threshold value enables precise measurements over a rather large energy range. This can be useful for certain types of measurements performed as part of the chip characterization[2], but in the final chips a smaller dynamic range that covers the MIP regime will be sufficient. In principle, having a precise value for the active thickness of the sensor, helps to have an idea about this MIP regime. For those working on the sensor simulations using generic doping profiles, confirming the active

[1] An 8-bit DAC corresponds to 256 possible discrete output levels.
[2] It for example enabled the measurement of the K_α peak in the ^{55}Fe spectrum for DAC calibration.

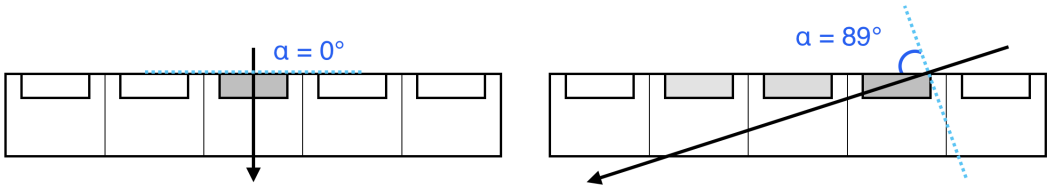

Figure 5.1: Ionizing particle (indicated by the arrow) interaction with a pixel sensor. Left: Orthogonal impact, charge collected in one pixel (gray). Right: Grazing angle impact, charge collected in multiple pixels, illustrating the grazing angle method. Denoted in blue is the rotational angle α. Varying shades of gray indicate the amount of charge collected by each pixel. Illustrations are not to scale.

thickness is particularly valuable, as this parameter is used as an input in the TCAD simulations. The more accurately this value is known, the better the simulations will reflect the actual sensor behavior, allowing for more reliable investigation of its properties [29].

5.2 Grazing angle method

The approach taken in this thesis to achieve the objective of measuring the charge collection profile of H2M is based on a technique called the *grazing angle method* [37]. This method allows to determine the charge collection profile by means of ionizing particles impinging the sensor plane under shallow angles, i.e. grazing angles. The charge generated in H2M when a particle impinges orthogonally, will be collected in about one pixel due to its relatively large pixel pitch of 35 µm and the small active thickness. In the grazing angle approach, where the particle impinges the sensor under shallow angles instead of orthogonally, the charged particle crosses several pixels, each one at a different depth. Therefore, the charge will be collected in several pixels and the charge collected in each of these pixels corresponds to the charge generated at a certain depth inside the sensor. The position in terms of location in the track can be translated into depth within the sensor, and thus the grazing angle measurements allow to determine the charge collection profile. A schematic illustration of the grazing angle approach can be found in Figure 5.1. This illustration shows an ionizing particle traversing a pixel sensor consisting of five pixels. On the left, the particle impinges orthogonally on the sensor, resulting in charge collection in a single pixel, which is highlighted in gray. On the right, the particle strikes the sensor at a shallow angle, causing charge collection across multiple pixels. This demonstrates the principle of the grazing angle method.
The angle between the sensor plane and the reference plane, shown as a light blue dashed line orthogonal to the particle trajectory, is indicated in blue in Figure 5.1. This angle is called the rotational angle α. The larger α, the more pixels will be crossed, and thus the better the sampling of the depth will be. The relation between rotational angle and the track length, i.e. the amount of pixels crossed by the particle, is shown in Figure 5.2. From this figure it also becomes clear that the grazing angle approach is only possible for rotational angles above about 80°; and if a reasonable sampling of the depth is desired, this angle should be no less than 89°. It is important to note that the angle at which particles must impinge upon the sensor for grazing angle measurements depends on the pixel dimensions. For pixel sensors with a smaller pixel pitch and/or larger active thickness than H2M, the required rotational angle to traverse

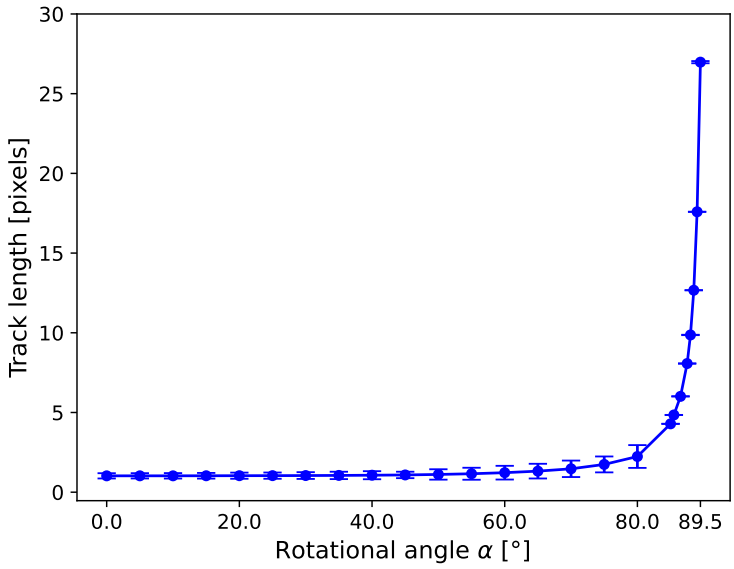

Figure 5.2: Track length as a function of rotational angle α.

a significant number of pixels may be less than 89°. As shown in Figure 5.2, a rotational angle of 89.5° corresponds to the particle crossing around 27 pixels. Assuming that the thickness of the active layer is about 10 µm, this comes down to a sampling step of about 0.4 µm.

5.3 Other possible approaches

The technique applied in this work is not the only possible method to investigate the active thickness of a silicon sensor. Other methods such as the *Edge Transient-Current Technique* or *Capacitance-Voltage Measurements* can also be applied to gain insight into the sensor's active region.

The Edge Transient-Current Technique (Edge-TCT) [38] for strip sensors, utilizes infrared (IR) laser pulses impinging at a certain depth parallel with the surface of the sensor and perpendicular to the strips. Changing the laser beam position, and thus the depth at which the carriers are generated, enables the measurement of collected charge as a function of depth within the sensor, i.e. the charge collection profiles. In principle this technique is also applicable for pixel sensors, however for example charge sharing between pixels can make the method less convenient. Apart from this, the biggest advantage of the grazing angle technique with respect to the Edge-TCT is the precision with which the active thickness can be determined. The spatial resolution of Edge-TCT measurements are limited by the employed optical system in the experimental setup. The width of the IR laser beam can be assumed to be multiple micrometers wide. This is not optimal when sampling an active thickness of about 10 µm. The grazing angle method, where sampling steps of sub micrometers can be achieved, is more suitable for the DUT in this work. In fact, for H2M this type of measurements is unfeasible simply due to the fact that a polished edge is required, which is currently not the case for the samples. Instead of impinging the sensor

from the edge, one can also consider illuminating the sensor from the top or back, to get an idea about the amount of charge collected in the epitaxial layer. Although, the H2M chip is suited for neither of these approaches as on the top of the sensor a metal stack of about 5 µm is placed and the about 40 µm thick substrate on the backside makes it complicated to focus the laser on the epitaxial layer.

In principle, Capacitance-Voltage (CV) Measurements can also be used to investigate the active thickness of a silicon sensor. Namely, as explained in Chapter 3, reverse biasing the sensor creates a depletion region, which behaves as a capacitor. The capacitance arising from this depleted region is inversely proportional to the width between "the electrodes", i.e. the depletion width [24]. Thus, measuring the capacitance when the sensor is fully depleted, allows to determine the depletion depth inside the sensor. As this reflects the region where an electric field exists, it is not accounting for charge collection via diffusion from undepleted regions. Thus, CV Measurement could be used to investigate the electrical structure inside the sensor, but is not suitable for a study of the full charge collection behaviour, which is the objective of this work.

6. Test beam measurements at DESY II Test Beam Facility

To determine the active thickness of H2M using the grazing angle method, the DUT must be exposed to a particle beam under shallow angles, as discussed in the previous chapter. For this purpose, the particle beam provided by the DESY II Test Beam Facility is used. This chapter outlines the experimental setup employed at the DESY II Test Beam Facility for the grazing angle measurements.

6.1 DESY II Test Beam Facility

The DESY II Test Beam Facility [39] is being operated at the DESY II synchrotron, installed in a tunnel located at the DESY campus in Hamburg. The primary function of DESY II is to serve as the last pre-accelerator stage for the PETRA III [40] synchrotron light source. Apart from accelerating electron or positron bunches to inject them into PETRA III, it is also used to generate electron or positron beams for the DESY II Test Beam Facility. The beams are generated by a double conversion instead of direct extraction of the primary beam in DESY II. The beam generation mechanism is illustrated in Figure 6.1. The first conversion takes place inside the DESY II synchrotron where carbon fiber targets are placed in the beam orbit. Interactions between the particle bunches and the target materials produce bremsstrahlung photons. These photons are then converted into electron-positron pairs using metal converter target plates. Three primary targets are positioned at different locations within DESY II, providing the test beam facility with three independent beam lines: TB21, TB22, and TB24, also visible in Figure 6.1. Each beam line is equipped with a dipole magnet whose polarity and magnetic field strength can be adjusted, allowing users to select the desired particle species, electrons or positrons, and momentum, ranging from 1-6 GeV/c. The uncertainty on the selected momentum is on the order of 5% [39]. The beams are characterized by a particle rate of up to 40 kHz and a divergence of approximately 1 mrad. The selected particles are collimated by the controllable primary collimator before they pass the beam shutter and enter the test beam area in which the experimental setup, including the DUT, is established. The shutter is controlled by a safety interlock system and enables safe access of the test beam area. Once the particle beam is turned on and data is being collected, the users cannot access the test beam area. To minimize radiation exposure, the test beam area is shielded by concrete blocks. To reduce the dose even further, additional beam dumps are installed in front of the concrete walls. The layout of these dumps varies across the different test beam areas. In the test beam area of TB22, in which all data investigated in this work has been recorded, the dump consists of an array of lead blocks at the wall. Once the beam is turned on, users are not permitted inside the shielded

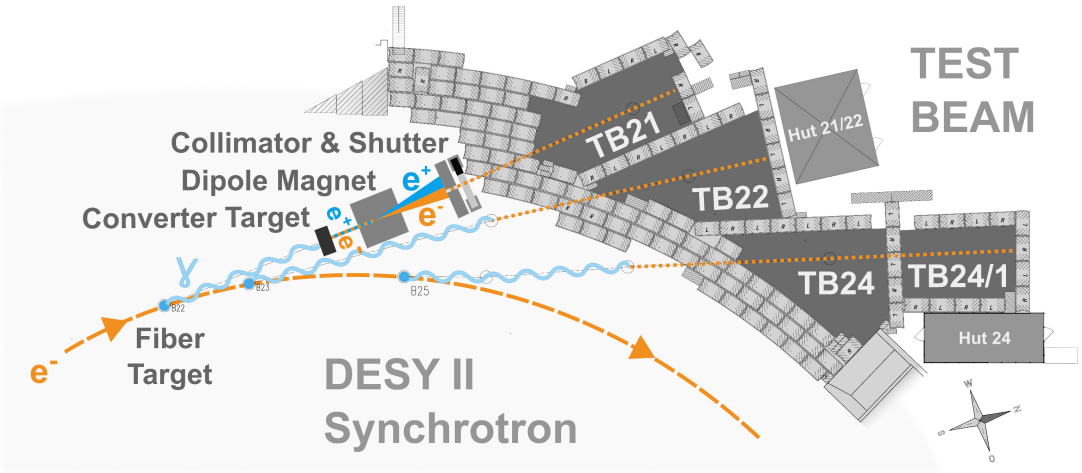

Figure 6.1: Generation of the particle beams at DESY II Test Beam Facility. Schematic representation taken from [39].

area and must remain in the designated control hut located outside the concrete barriers, as indicated in Figure 6.1. Once the beam particles passed the shutter, they cross an exchangeable fixed-size secondary collimator which enables further collimation of the beam via lead insets with different bore diameters and shapes. The one utilized for generating the data analysed in this thesis was 12 mm × 18 mm. The test beam areas are equipped with essential infrastructure for the testing of nuclear and particle physics detectors. The infrastructure available in each of the three test beam areas differs slightly. In test beam area TB22 an ADENIUM [41] beam telescope consisting of ALPIDE planes [28] is installed as a reference system to register the location and timing of the passing particles. Global trigger signals and synchronization of the data acquisition by different devises of which the experimental setup is comprised, are provided by the AIDA Trigger Logic Unit (TLU) [42]. For mechanical integration of the DUT, a x-, y-, α-stage system with sub-µm- and sub-degree precision is provided. A more detailed description of the functionality and interconnections of these systems is provided in Section 6.2.

6.2 Experimental setup

The experimental setup used to conduct the measurements listed in Chapter 7 is shown in Figure 6.2. Denoted in yellow is the the particle beam, directed from right to left. Indicated in green is the DUT, H2M, which is mounted onto the position stage. The DUT is positioned in the middle of the ADENIUM beam telescope, with three ALPIDE telescope plane, denoted in blue, on either side. In red TelePix2 [43], which is used as a Region-of-Interest (ROI) and trigger plane, is indicated. Not visible in this image are the AIDA-TLU, power supplies, and bias voltage sources for sensor biasing of TelePix2 and H2M. In the following, selected components are discussed in greater detail, along with the description of their interconnection and the data-taking methodology.

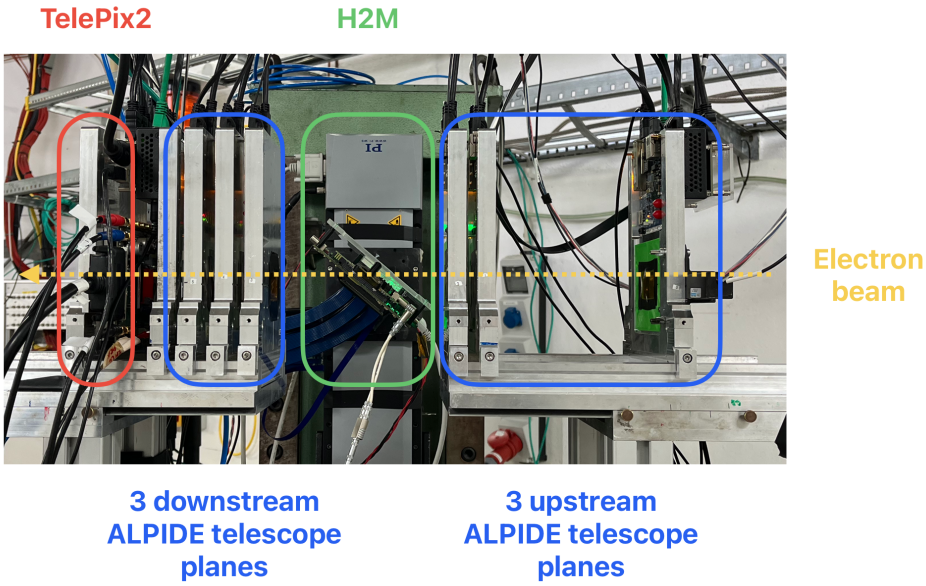

Figure 6.2: Lateral view of the experimental setup employed at TB22 of DESY II Test Beam Facility to conduct the measurements listed in Chapter 7.

6.2.1 Integration of H2M

For data acquisition, the H2M chip is integrated into the Caribou DAQ system [44], an open-source project encompassing hardware, software and firmware specifically designed for pixel detector development. The hardware part of the system consists of three boards: the *System-on-Chip (SoC) board* on which software (Peary) and firmware for the configuration, control and readout of the chip are running, the *chip board* containing the sensor (H2M in this work), and the *Control and Readout (CaR) board* which provides current and voltage sources and physically connects the SoC and chip board. The chip board is application-specific. Remarkable about the H2M chip board is the way in which the chip is mounted onto the board. As can be seen in Figure 6.3, the chip is only partially attached to the Printed Circuit Board (PCB), such that its active area extends beyond the edge of the board and is not enclosed by PCB material. As a result, rotating the chip to grazing angles does not increase the material budget in the particle beam trajectory, since the chip board configuration prevents any PCB material from entering the beam path. This makes the H2M chip especially suitable for grazing angle studies.

As previously mentioned, the DUT is mechanically integrated into the experimental setup using a position stage system that enables adjustments of its orientation. In the following, the orientation of the DUT is consistently described in terms of the orientational angle α, defined in Chapter 5 as the angle between the DUT plane and a reference plane perpendicular to the particle trajectory. Figure 6.4 illustrates the definition of α based on a photograph of the experimental setup. Although this definition may appear unintuitive in the context of grazing angle measurements — which focus on the small angle between the sensor plane and the particle trajectories — it was adopted to reflect the natural choice of assigning $\alpha = 0°$ to the standard configuration, where the DUT plane is perpendicular to the particle trajectory. As the DUT

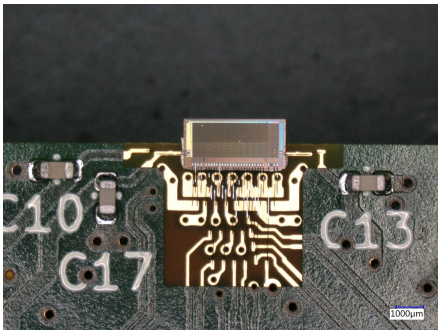

Figure 6.3: Image of H2M attached to its chip board. The active area of the chip exceeds the PCB edge.

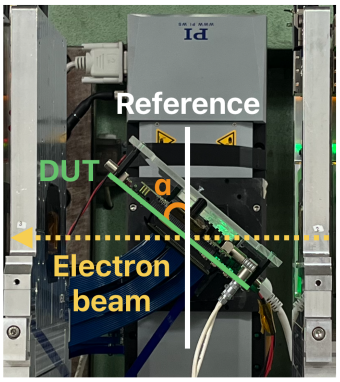

Figure 6.4: Definition of the rotational angle α, denoted in orange.

is tilted, α increases, and a grazing angle configuration is reached when the DUT is rotated to approximately 90°, that is, when the sensor plane is nearly parallel to the beam direction.

6.2.2 ADENIUM beam telescope

Beam telescopes provide precise spatial information about the trajectories of the beam particles as they cross the DUT. This information serves as a reference, against which the response recorded by the DUT can be compared. By correlating the reconstructed particle tracks with the DUT measurements, the performance of the DUT can be investigated. As precise detector alignment is necessary for the performance evaluation of the DUT, but was found to be unachievable at grazing angles, the telescope data are excluded from the final analysis presented in this work. Nevertheless, beam telescope data were recorded, and a discussion of the instrumentation used for this is presented in this section.

The ADENIUM beam telescope [41] (ALPIDE sensor based DESY Next test beam Instrument) consists of six ALPIDE telescope planes. These sensors exhibit a pixel matrix of 512×1024 pixels with a pixel pitch of $26.88\,\text{mm} \times 29.24\,\text{mm}$. This comes down to a sensitive size of $13.8\,\text{mm} \times 29.9\,\text{mm}$. The sensors together with their DAQ hardware components are fixed in an aluminum box featured with a hole at the location of the sensor to minimize the amount of material budget in the beam. To protect the sensors from dust, the openings are covered by polyimide sheets on both sides. Figure 6.5 presents a photograph of H2M (right, foreground) positioned between the telescope planes (left, background). The aluminum enclosure and the protective sheet over the opening are clearly visible. Furthermore, the image illustrates the notable difference in sensitive area between the DUT and the telescope sensors, which will become important in the next section.

The telescope planes are mechanically integrated onto rails arranged into two arms parallel to the beam axis. This allows independent movement of the planes and thus enables a flexible layer arrangement. The six planes are organized in two groups of three, separated by the DUT. The telescope planes which are crossed by the beam particles before they reach the DUT are called the upstream planes; the planes which are crossed after the particles traversed the DUT

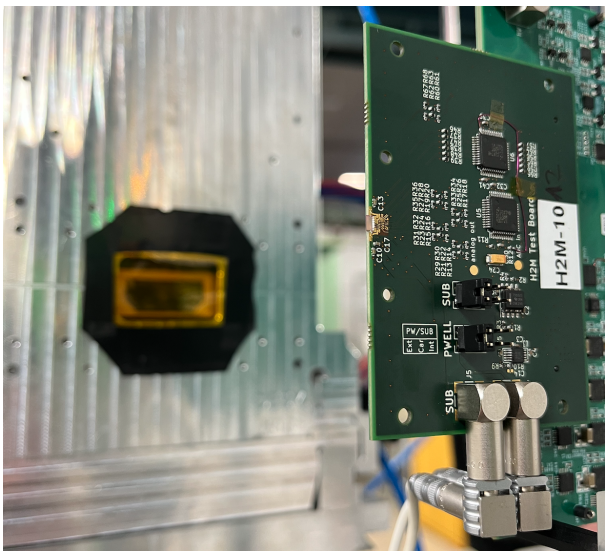

Figure 6.5: Photograph of H2M (right, foreground) and an ALPIDE telescope plane (left, background), illustrating the notable difference in sensitive area between the two sensors.

are called the downstream planes, as also denoted in Figure 6.2.
As will be discussed in Chapter 7, the data investigated in this work originates from two test beam campaigns conducted at the DESY II Test Beam Facility, one in May 2024 and another one in February 2025. In both campaigns, a different configuration of the telescope planes was employed; schematically represented in Figure 6.6. The configuration from May 2024 was optimized for track reconstruction. However, analysing the data from the first campaign revealed problems in the alignment of the DUT oriented under grazing angles. Therefore, during the second campaign, the arrangement was slightly changed; in principle still suited for determination of the angle with which the incoming beam particles strike the sensor, but less suited for the determination of the angle at which they leave the DUT. Closing the last telescope plane also enabled the placement of TelePix2—located immediately after the last telescope plane—closer to the DUT, which makes it possible to better define the ROI.

A notable difference between the standard telescope configuration and the setup required for grazing angle measurements lies in the spacing between the DUT and the two innermost telescope planes. When the DUT is positioned perpendicular to the beam axis, the telescope planes can be placed relatively close to the DUT, thereby achieving excellent tracking resolution. In contrast, for measurements at grazing angles, the DUT must be tilted significantly, necessitating an outward displacement of the telescope planes to accommodate the PCB supporting the DUT between them.

6.2.3 AIDA-TLU and ROI triggering with TelePix2

For efficient data taking, it is essential to record only those events in which a particle has passed through the DUT. To select such events, a trigger system is employed. Since the ALPIDE sen-

Figure 6.6: Schematic illustration of the telescope arrangement used during the two test beam campaigns: the May 2024 campaign at the top and the February 2025 campaign at the bottom.

sors are substantially larger than the H2M sensor, triggering on the telescope planes[1] would lead to a high rate of events where no particle actually intersects the DUT. Although the beam particle passed through the larger active areas of the telescope planes, it often missed the much smaller active area of the DUT, resulting in the recoding of many empty DUT frames. Consequently, unnecessary storage is occupied by irrelevant events and the time required for data processing is increased. This issue can be solved by adding TelePix2 [43] as a Region-of-Interest (ROI) trigger layer. The pixel matrix of TelePix2 consists of 120×400 pixels with a pitch of 165×25 µm^2, resulting in a total active area of 2×1 cm^2. For the integration of TelePix2 in the setup, the same mechanical structure as the telescope planes is utilized. The sensor is placed behind the most downstream ALPIDE telescope plane, as can be seen in Figure 6.2 and Figure 6.6. The concept of ROI triggering with TelePix2 is based on the trigger window which can be configured to any pixel arrangement. The pixels of TelePix2 which overlap with the active area of the DUT, are left unmasked, whereas the others are masked. When a beam particle crosses the ROI, a fast digital signal, called the HitBus, is sent to the trigger logic unit, and the telescope planes and DUT are read out. The trigger window selected on TelePix2 is defined slightly larger than the DUT sensor to ensure high statistics even at the edges of the DUT. The size of the window depends on the DUT orientation, as the projection of the DUT's sensitive area onto the TelePix2 plane varies with the angle between them. The projected area is maximal when the DUT is parallel to TelePix2, corresponding to an orientation characterized by a rotational angle of 0°. As the rotational angle of the DUT increases, the projected active area on TelePix2 decreases. This effect is illustrated in Figure 6.7, showing the hitmaps of the most downstream telescope plane for two DUT orientations: 0° (left) and 89.5° (right). The gradient observed within the ROI is caused by the positioning of the particle

[1]This is a theoretical scenario; in practice, the telescope planes do not provide a trigger signal required for the triggering procedure.

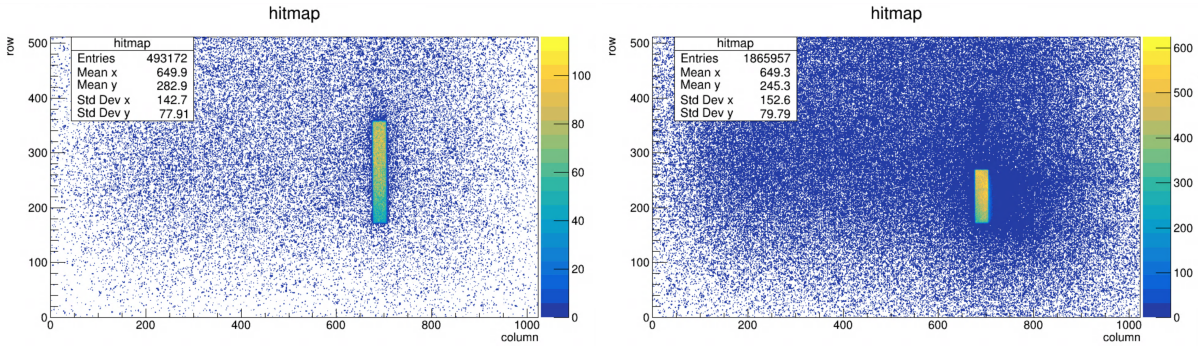

Figure 6.7: Hitmaps of the most downstream telescope plane for two DUT orientations, 0° (left) and 89.5° (right), demonstrating how the selected Region-of-Interest shifts with orientation.

beam, which appears to be shifted slightly upward. Additionally, the hitmap corresponding to the 89.5° orientation shows an increased amount of hits outside the ROI, suggesting the presence of more scattering in this configuration. During the test beam campaigns, it was necessary to adjust the selected trigger window to optimize data-taking efficiency for each DUT orientation.

The communication between TelePix2 and the other detectors in the experimental setup, is taken care of by the AIDA-TLU [42], as schematically represented in Figure 6.8. Trigger logic units are used to implement a logical combination of the incoming trigger signals and produce a corresponding global trigger output that is distributed to the DUT and telescope planes. In the employed setup, the only trigger signal is coming from the TelePix2 HitBus, so the logic implementation is as follows: if a hit occurs in the selected trigger window on TelePix2, then a global trigger signal is sent to H2M and the ALPIDE telescope planes. Additionally, the TLU provides TelePix2 and the Caribou system with a start signal (t_0) for synchronization and a clock (40 MHz for Caribou and 125 MHz for TelePix2 readout clocks) to assign timestamps for the trigger signals. When the TLU recieves a valid trigger signal from TelePix2 (trigger in), it sents out a global trigger signal (trigger out). As a response to the reception of the trigger signal from the TLU, the ALPIDE telescope planes and DUT send back a busy signal, indicating that they are performing the readout of the previous event, and thus are unavailable for a new trigger. As long as the busy signal holds, triggers are vetoed. Figure 6.8 provides a schematic overview of the interconnections between the setup devices. All devices are fully integrated in the EUDAQ2 [45] data acquisition framework.

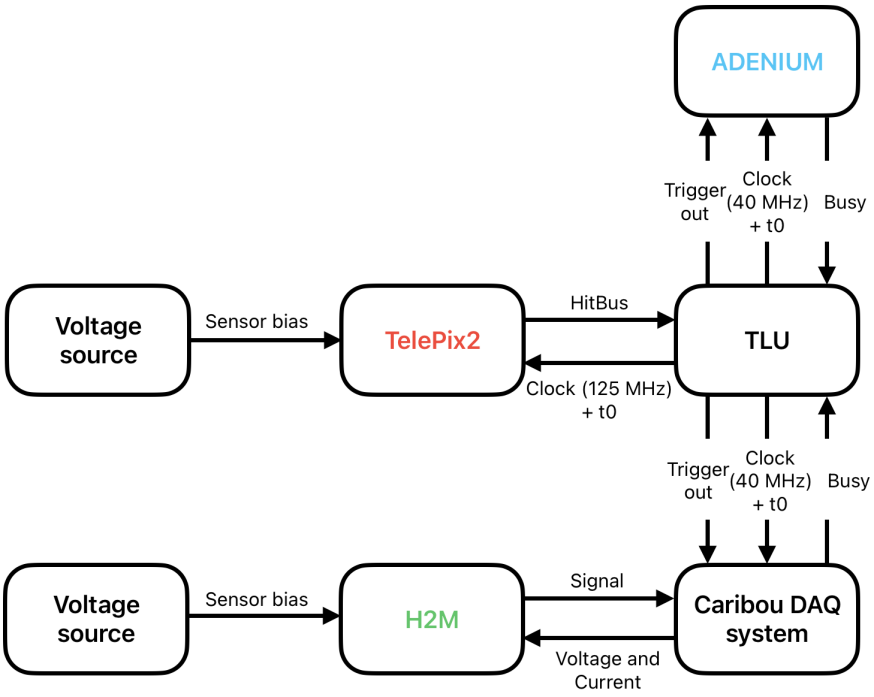

Figure 6.8: Schematic overview of the interconnections between the different setup devices.

7. Data collection and description

The experimental data presented in this thesis originate from two test beam campaigns: one conducted in May 2024, referred to as dataset 1, and another in February 2025, referred to as dataset 2. In addition to the differences in the experimental setup, as discussed in Section 6.2, the two datasets exhibit further distinctions. The aim of this chapter is to clarify these distinction and give a comprehensive overview of all collected data.

7.1 Dataset 1

The data contained in dataset 1 was collected in May 2024, when the concept of rotating the DUT relative to the beam to determine the active thickness was well understood. However, the exact analytical approach to achieving this result had not yet fully been established. Consequently, the optimal DUT orientation for measuring the active thickness was unknown, necessitating the investigation of multiple rotational configurations. Both full range and grazing angle scans were performed. The angles at which data is collected are specified in Table 7.1. The most relevant data for grazing angle studies was collected at an angle of 89.5°. The idea of collecting full range angle scans, in which the DUT is systematically rotated from 0° to 90°, was to facilitate the alignment procedure and systematic selection of the region of interest of Telepix2. Analysing dataset 1 underscored the importance of collecting sufficient data for a successful analysis. This insight was applied in the second test beam campaign, where the focus shifted to gathering high-statistics data at grazing angles.

All data in dataset 1 was obtained from H2M-2 with a nominal thickness of 50 µm. To reduce scattering, the protection cover was removed when data was collected at grazing angles. The particle beam consisted of electrons with a momentum of about 4.8 GeV/c.

Table 7.1: Overview of investigated angles in dataset 1.

Type of data	**Angle range**	**Steps**
Full angle scan	-20° - 90°	5°
Grazing angle scan	89.5° - 87.5° 87.5° - 89°	1° 0.5°
Grazing angle	89.5°	/

7.2 Dataset 2

During the second test beam campaign, samples with a reduced total thickness were available. These samples were produced in a single-die thinning process. Since only about 10 µm of the 50 µm of H2M is epitaxial layer, further thinning of the chip is in principle possible without significant performance loss. Interest in this thinning procedure comes from the fact that samples with a reduced total thickness have the benefit of a reduction in material budget, which is important for tracking applications, and the ability to illuminate the sample from the backside with low-energy X-rays.

The data contained in dataset 2 was obtained from H2M-8, which has a reduced total chip thickness of 25 µm. For precautionary reasons, the protection cover of H2M-8 was not removed for the grazing angle measurements. As a result, the electrons had to pass through additional material before reaching H2M, which introduced more scattering leading to an increased angular spread of the electron beam. Consequently, unlike in May 2024, the optimal setup angle in February 2025 was 89° instead of 89.5°. To investigate the difference in letting the beam impinge the sensor from the surface or backside, data was taken both at 89° and 91°. Additionally, data was recorded at a rotational angle α of 0°, which is essential for determining the active thickness of the sensor in the analysis. Compared to dataset 1, dataset 2 does not contain a full range angle scan to facilitate the detector alignment procedure, since if was found from the analysis of the first dataset that the alignment is unfeasible at grazing angles, even if it is performed systematically. Beyond investigating the impact of different incident angles, the effect of varying chip parameters was also examined. Data was collected at three different sensor bias voltages ($-0.8\,\mathrm{V}$, $-1.2\,\mathrm{V}$ and $-3.6\,\mathrm{V}$ were applied) and two hit detection threshold settings (of approximately 300 and 400 electrons). The beam with which the sensor was impinged in the second test beam campaign consisted of electrons with a momentum of about 4.6 GeV/c.

An overview of the collected data, highlighting the key differences between the two datasets, is provided in Table 7.2.

Table 7.2: Overview of collected data from two test beam campaigns, highlighting variations in dataset content and the experimental conditions, including sample properties, under which they were generated.

Dataset	**Test beam campaign date**	**Sample**	**Total chip thickness**	**Electron beam momentum**	**Content description**
1	May 2024	H2M-2	50 µm	4.8 GeV/c	- Data collected without protection cover - Various different angles - Lower statistics per setting - Systematic changes in applied sensor bias voltage
2	February 2025	H2M-8	25 µm	4.6 GeV/c	- Data collected with protection cover - Data taken at 89°, 91° and 0° - Higher statistics - Both systematic changes in applied sensor bias voltage and hit detection threshold

8. Data analysis strategy

This chapter provides a detailed description of the methodology used to extract the charge collection profiles from the collected data. The analysis follows a two-step process. First, the raw data from the test beam campaign is processed using the Corryvreckan software to generate structured data. In the second step, these structured data serve as input for the analysis code, which produces the final results: charge collection profiles that enable the investigation of charge collection at different sensor depths and the determination of the active thickness.

8.1 Corryvreckan software

Corryvreckan is a software designed for offline reconstruction and analysis of test beam data [46, 47]. It has a modular structure, making it relatively accessible, and is highly configurable. Corryvreckan is released as free and open-source software under the MIT license, with the source code available through the project's software repository [48]. Rather than presenting an exhaustive description of the software, this section aims to summarize its role and usage within the scope of this work. All details can be found in the comprehensive user manual accessible at [46], which also serves as a primary reference for the descriptions of all used modules and parameters in the following.

To run the software, the user must provide two main input files: a geometry file and a configuration file. The *geometry file* contains a full geometry description of the test beam setup. The number of devices and their types as well as their position and orientation, along other essential properties for the reconstruction, are specified. An example of a geometry file, describing a detector setup consisting of six telescopes planes, one trigger layer and the DUT, is given below.

```
[adenium_0]
orientation = -0.542476deg,179.17deg,-0.515777deg
position = -1.09061mm,69.719um,8mm
type = "adeniumrawdataevent"
...

[TLU_0]
type = "tlu"
...

[adenium_1]
orientation = 0.983597deg,180.467deg,0.150974deg
position = -162.626um,487.652um,156mm
type = "adeniumrawdataevent"
```

```
...

[adenium_2]
orientation = 1.7466deg,180.269deg,-0.101815deg
position = -537.743um,94.913um,183mm
type = "adeniumrawdataevent"
...

[H2M_0]
mask_file = "/scratch/feyens/masks/masking_3V6.txt"
orientation = 179.175deg,90.0579deg,89.7795deg
position = -5.97292mm,-314.378um,270mm
type = "h2m"
...

[adenium_3]
orientation = 0deg,180deg,0deg
position = 0um,0um,349mm
type = "adeniumrawdataevent"
...

[adenium_4]
orientation = 0.745991deg,179.24deg,-0.139057deg
position = -647.891um,77.412um,376mm
type = "adeniumrawdataevent"
...

[adenium_5]
orientation = -2.29871deg,181.814deg,-0.1017deg
position = -878.829um,-137.697um,519mm
type = "adeniumrawdataevent"
...
```

Each detector is described in a separate section, which starts with a header describing the name used to identify the detector which is denoted between square brackets. Several parameters can be contained in the section. Only four were displayed here:

- The `orientation` defines the Euler angles relative to the global axes, which are defined by a right-handed Cartesian system with the z-axis parallel to the beam direction and the origin defined by the placement of the detectors in the geometry of the setup.
- The `position` defines the position of the geometric center of the detector given in the global coordinates. The z-coordinates are also denoted in Figure 6.6.
- The `type` parameter describes the type of detector, such as `adeniumrawdataevent` for the ADENIUM telescope planes and `h2m` for the DUT.
- The `mask_file` parameter in `[H2M_0]` allows specific pixels to be masked during offline reconstruction, excluding noisy and inneficient pixels.

The *configuration file* includes several sections that define the modules to be used. These modules, denoted between square brackets, are executed in the order in which they are defined in the file. The first module which is called is the `[Corryvreckan]` module. It provides a global set of parameters which are inherited by all modules. The defined parameters can be seen below.

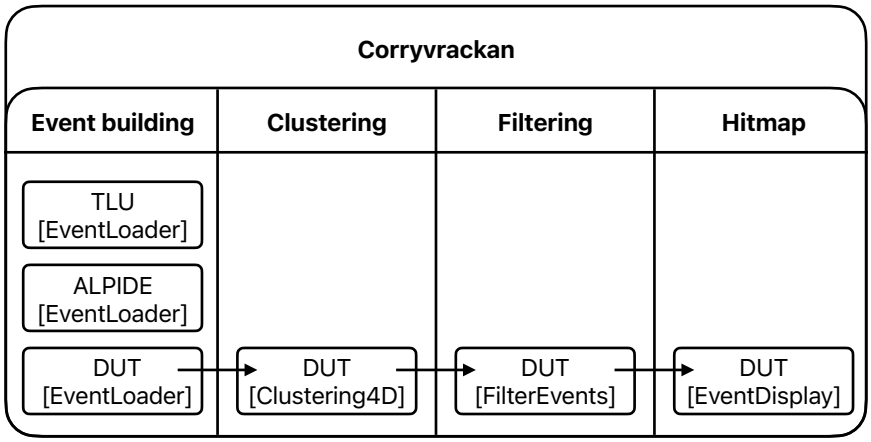

Figure 8.1: The Corryvreckan workflow, which transforms raw test beam data into structured data used in the second stage of the analysis.

```
[Corryvreckan]
detectors_file = geo/geometry.geo
detectors_file_updated = geo/geometry_updated.geo
histogram_file = dut_analysis.root
```

The `detectors_file` identifies the location of the file describing the detector configuration. The `detectors_file_updated` specifies the path to the file where the potentially updated detector configuration should be saved. Also the `histogram_file` is provided, which gives the location of the file where the ROOT output histograms of all modules will written be to.

The modules that follow the global framework are associated with partitioned functionalities within the software system. Figure 8.1 provides the workflow as defined by the modules in the configuration file used to organize the test beam data in this thesis. Four steps are undertaken in order to go from raw test beam data to the structured data used as an input for the second part of the analysis.

The first step in the reconstruction process is event building, where data corresponding to the same physical interaction from different subsystems of the detector setup are combined. This grouped data is referred to as an event. The module `[EventLoaderEUDAQ2]` is used to import raw detector data recorded by EUDAQ2 into Corryvreckan in the form of such events. A separate event loader section is configured for each detector type, as shown below.

```
[EventLoaderEUDAQ2]
type = "h2m"
file_name="/tb_desy_202404/data/run000962_h2m_231107193741.raw"
eudaq_loglevel = "INFO"
log_level = "INFO"
```

```
acq_mode = 1
calibration_path_tot = /calibration_files/fit_parameters_h2m2_3V6_thr111.txt
...

[EventLoaderEUDAQ2]
type="tlu"
file_name="/tb_desy_202404/data/run000962_tel_231107193807.raw"

[EventLoaderEUDAQ2]
type = "AdeniumRawDataEvent"
file_name="/tb_desy_202404/data/run000962_tel_231107193807.raw"
```

The `type` parameter specifies the detector type to which the section applies, and `file_name` defines the corresponding raw data file. Additional parameters, such as `eudaq_loglevel` and `log_level`, can be used to enable verbose output of EUDAQ2 and Corryvreckan, respectively. Some parameters are specific to particular detector types, such as those found in the H2M section. For example, `acq_mode` defines the readout mode in which H2M is being operated; a value of 1 indicates that data were recorded in ToT mode. The `calibration_path_tot` parameter provides the calibration file needed for the threshold and ToT calibration, as will be discussed in Section 8.2.6.
The output of these modules are several 1D and 2D histograms, one of which are the hitmaps, displaying the amount of detector hists recorded at different location within the detector. An example of such a hitmap was already shown in Figure 6.7 of Chapter 6 to illustrate the dependence of the selected trigger window on the orientation of the DUT.

Once the raw data are loaded, the structuring can start. This is performed via a procedure known as clustering, in which the detected hits in the detectors are grouped into clusters based on their spatial and temporal proximity. The amount of pixels grouped into one cluster identifies the size of that cluster, referred to as the cluster size. The total amount of charge, i.e. the sum of the amount of charge collected in all pixels comprising that cluster, identifies the cluster charge. For the clustering, the `[Clustering4D]` module is used. The provided parameters are again shown below.

```
[Clustering4D]
use_earliest_pixel = true
reject_by_roi = true
neighbor_radius_col = 3
neighbor_radius_row = 3
...
```

By setting the `use_earliest_pixel` parameter to true, the pixel with the earliest timestamp is used to set the cluster timestamp. By enabling the `reject_by_roi` the clusters positioned outside of the ROI defined for the telescope planes, will be rejected. The latter two parameters, `neighbor_radius_col` and `neighbor_radius_row`, determine the search radius for neighbouring pixels in column an row direction, respectively. By increasing the default value of 1 to 3, split clusters are being allowed.
Again, for each detector multiple plots are produced. Those that are of interest in this thesis are the cluster size and cluster charge histograms. A distinct histogram is generated for the

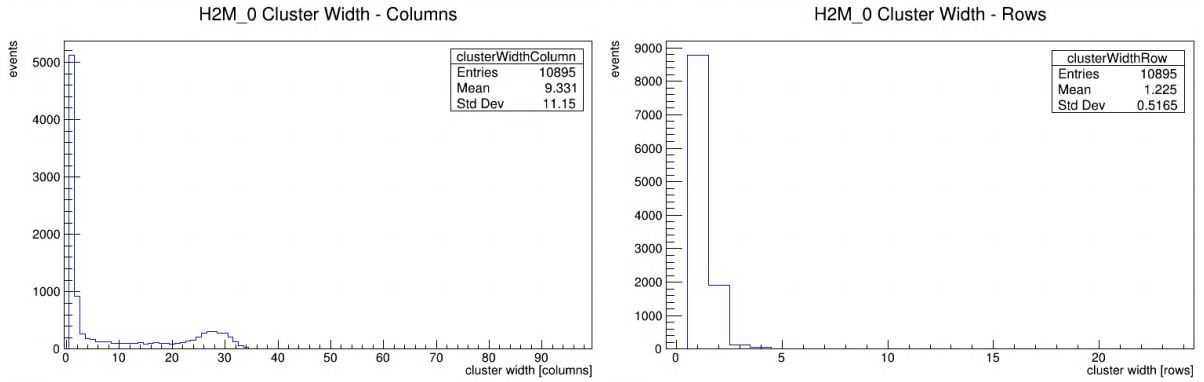

(a) (b)

Figure 8.2: Cluster size histograms for both directions of the DUT: (a) the column/x direction and (b) the row/y direction. The represented data was generated at an orientational angle of 89.5°.

cluster size along the columns/x and rows/y direction. An example of both of these histograms can be seen in Figure 8.2. The analysed data represented in these histograms is generated at grazing angles. The cluster size is significantly larger along the column direction than along the row direction, indicating the direction in which beam particles traversed multiple pixels of the DUT due to its tilted orientation.

As discussed in Chapter 5, this work focuses on events characterized by large cluster sizes, as this indicates that multiple pixels were traversed by the beam particle, providing better depth sampling. To select such events, the `[FilterEvents]` module is used. As the name implies, it filters events based on criteria such as cluster size.

```
[FilterEvents]
filter_duts = true
min_cluster_size = 20
```

By enabling the `filter_duts`, the detectors identified as DUT are taken into account for the filtering. The value provided for the `min_cluster_size` parameter defines the minimum size a cluster must have in order to pass the filtering. The chosen value is motivated by the distribution shown in Figure 8.2a, which demonstrates that applying a cut at 20 selects events with the largest cluster sizes while retaining sufficient statistics for the analysis. For all recorded data the `min_cluster_size` was set to 20, apart from the data recorded at 91°, where the high statistic events were shifted to lower cluster size values and a cut at 15 was employed. Of the total amount of recorded events, about a percent passed the filtering.

Once the useful events are selected, they can be visualised using the `[EventDisplay]` module. As can be seen below, this module does not take any parameters.

```
[EventDisplay]
```

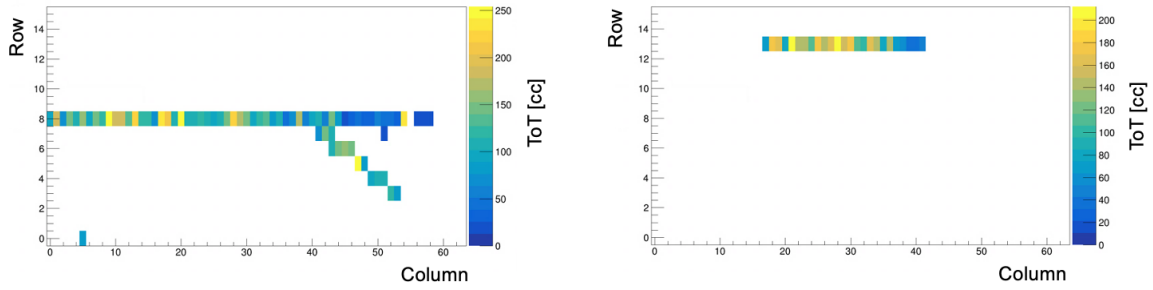

Figure 8.3: Examples of `[EventDisplay]` output for the H2M detector, displaying tracks.

As an output it generates for each detector 2D histograms of the pixel raw data, also referred to as hitmaps. Examples of these hitmaps can be seen in Figure 8.3. The hitmaps generated by the `[EventDisplay]` module, show the trajectory of the particle through the sensor. Therefore, in the following, the clusters shown in the hitmaps will also be referred to as *tracks*.

8.2 Grazing angle analysis

The hitmaps of the filtered events generated using the Corryvreckan software are taken as an input for the analysis code, which is based on the analysis described in [37], performing the second part of the analysis. This second part consists of several steps.

8.2.1 Selection of the preferred events

As a first step, the preferred events are selected. These are the events which meet the following two conditions:

1. No hits are appearing in the first and last column of the DUT. Events where hits are appearing in these columns are discarded to ensure that only completely recorded tracks are taken into account in the analysis.

2. Hits are only appearing in one or two adjacent rows. Events where hits appear in more than two rows are discarded, as they suggest the presence of δ-electrons. Figure 8.4 shows the ToT hitmaps of two events, illustrating the difference in the ToT pattern generated by a particle with and without δ-electron. In both events the ionizing particle is entering the sensor from the left side and crossing the sensor from top to bottom. In the event represented on the left side, a δ-electron is present in the beginning of the track where ToT values are measured in more than two rows. In the event displayed in the right hitmap, hits are occurring in precisely two adjacent rows. This is due to charge sharing, which is more present in the deeper regions in the sensor, so at the end of the track. A comparison of both hitmaps shows that allowing hits in two adjacent rows is justified and does not introduce δ-electron events into the analysis.

About 50 % (dataset 2) to 60 % (dataset 1) of the filtered events are found to meet the conditions of preferred events.

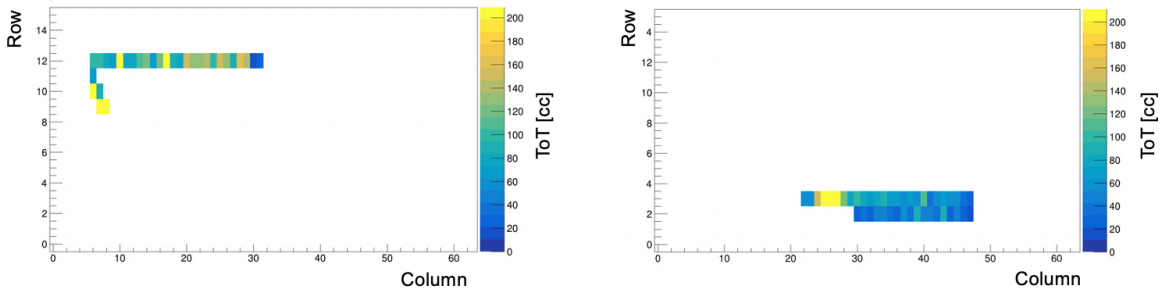

Figure 8.4: H2M hitmaps showing ToT values. Left: the presence of a δ-electron at the beginning of the track is visible—this is an example of a discarded event. Right: event where hits are occurring in two adjacent rows caused by charge sharing in the deeper regions of the sensor—this represents an event that is accepted.

8.2.2 Event classification by track length and particle trajectory direction

All selected preferred events are classified based on their track length and particle trajectory direction. For both classifications, the ToT hitmaps of the preferred events are projected onto the x-axis, resulting in a 1D distribution of ToT values along the columns of the DUT. The start of the track is defined as the firing pixel with the lowest column coordinate. The projection (sum of ToT values along the column direction) thus represents the pixel response as a function of the pixel position with respect to the track start. An example of such a projection is shown in blue in Figure 8.5. The track length generated by the traversing particle is defined as the number of non-empty bins in the projected distribution. Using the projection rather than the hitmaps to count non-empty entries for the track length determination improves the accuracy of track length definition for events in which hits are appearing in two adjacent rows. Namely, the track length should reflect the sensor's depth sampling, which occurs along the x-axis of the chip, as demonstrated in Figure 8.2. In other words, charge collected in adjacent columns originates from different depths, whereas charge collected in adjacent rows comes from the same depth. Therefore, independently counting hits in adjacent rows would wrongly increase the track length value and thus overestimate the depth sampling corresponding to the track length. The necessity of classifying events based on track length will become clearer in Section 8.2.3. In essence, this classification ensures that when combining multiple events with the same track length, the resulting statistics represent the same depth within the sensor.

The distribution of determined track lengths varies with chip settings (different sensor bias voltage and hit detection threshold). For most settings, events with a track length of approximately 28 pixels were most common when the DUT was oriented at a rotational angle of 89° or 89.5°. Apart from data collected at 91° (dataset 2), which showed a shorter dominant track length of around 16 pixels. Typically, about 8–20 % of preferred events at a given setting exhibit the most common track length. While most settings showed around 8 %, dataset 1 and the data taken at 91° from dataset 2 showed higher proportions of 15 % and 20 %, respectively. The absolute number of such events depends on the initial size of the dataset; generally, around 1,000 preferred events per setting shared the same track length. Sometimes this number was 3 to 6 times higher, but in all cases, the statistics were sufficient for reliable analysis. It was

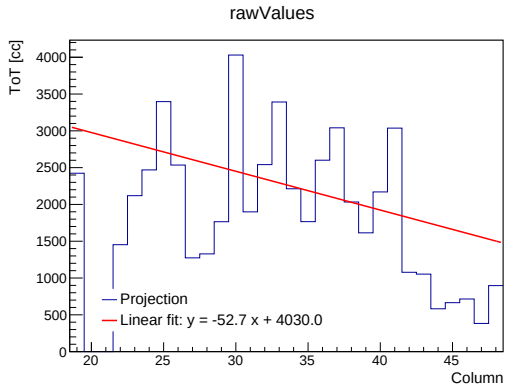

Figure 8.5: Projection with corresponding linear fit of a downgoing event recorded at a rotational angle of 89.5°.

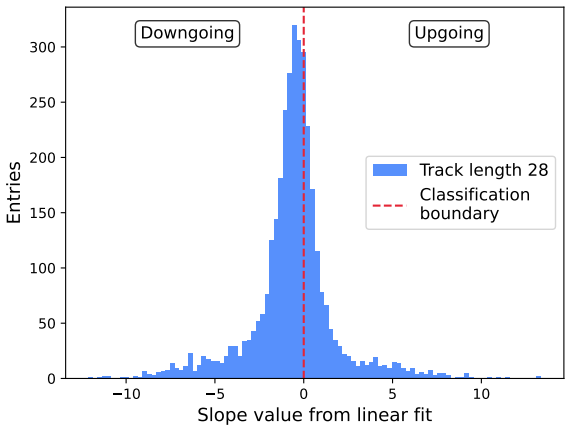

Figure 8.6: Distribution of slope values obtained from linear fits through the projections of events recorded at 89.5°.

also found that, in addition to the most common track length, one or two adjacent longer and shorter track lengths also contained sufficient statistics for a reliable analysis.

As previously discussed in Chapter 6 and Chapter 7, beam particles can enter the sensor from two directions: either from the surface (electronics side) and exit through the backside (substrate side), or vice versa—from the back to the surface. Particles entering from the surface are referred to as *downgoing*, while those entering from the backside are called *upgoing*. In grazing angle measurements, where the angle between the particle beam and the sensor is on the order of 1° or smaller, the distinction between upgoing and downgoing particles can become ambiguous. This is due to the beam's intrinsic divergence, as well as potential scattering in materials encountered before reaching the sensor. As a result, some particles may follow a trajectory opposite to what is expected based on the sensor's orientation—i.e., particles which should enter the sensor from the surface by orientation of the chip, actually enter from the backside; or vice versa. The essential difference between the two types of events is the order in which the active thickness of the sensor is sampled. In order to not only determine the total active thickness of the sensor, but also preserve the information of charge collection as a function of depth within the sensor, both types of events should be separated.

This distinction is again based on the projection of the ToT hitmaps of the preferred events, but in this case, a linear fit is applied to the projection. The resulting slope of the fit allows for classification of the particle's direction: when beam particles cross the sensor from left to right (i.e. from lower to higher column values), a negative slope indicates entry from the surface—corresponding to a downgoing particle—while a positive slope indicates entry from the backside, corresponding to an upgoing particle. In Figure 8.5 an example of such a projection with corresponding linear fit of a downgoing particle is shown.

Figure 8.6 shows the distribution of slope values obtained from linear fits applied to the projections of events recorded at 89.5° (dataset 1). The classification boundary, corresponding to

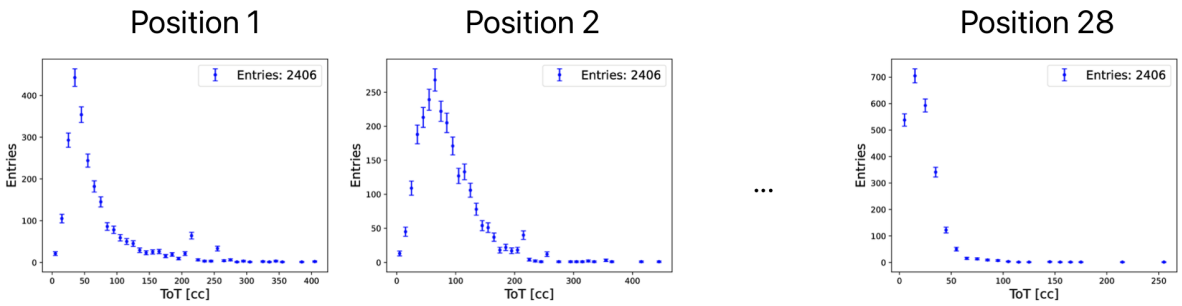

Figure 8.7: Signal distributions at various positions along downgoing track with track length 28. The total number of entries is indicated; however, not all are explicitly visible due to rebinning.

a slope of zero, is indicated in red. A greater number of events have negative slope values, classifying them as downgoing particles, which is consistent with the DUT's orientation. Overall, approximately 70 % of the preferred events with a given track length are identified as downgoing. An exception is the data taken at 91°, where around 80 % of the events are classified as upgoing, again as expected based on the orientation of the DUT.

8.2.3 Building and fitting the signal distributions

The next step is to build and fit the signal distributions. This step is applied separately to all groups of events defined by a specific track length and particle trajectory direction. For clarity, downgoing events with a track length of 28 are used as an example. The first step in building the signal distributions is the creation of 64 histograms. This amount corresponds to the maximum possible track length of an event due to the dimensions of the pixel matrix of the DUT, which has 64 columns. The first histogram is filled with the ToT values in clock cycles (cc) of the first pixels of all downgoing tracks with a track length of 28. The second histogram is filled with the ToT values of the second pixels, and so forth, until the last pixel of the tracks is reached, which is in this example pixel number 28. All remaining histograms remain empty and are not further used. Examples of the constructed histograms, referred to as the signal distributions, are shown in Figure 8.7. The position number above the shown distributions refer to their corresponding position in units of pixel number in the track. Thus, the signal distributions represent the distribution of recorded ToT values at different positions, denoted by pixel number, in the track. The uncertainties quoted in the signal distributions are the Poisson uncertainties determined by Corryvreckan.

The collected charge, in terms of ToT, is measured by performing a fit with a Landau curve convoluted with a Gaussian, as described in Section 3.1, to the signal distributions. The Most Probable Value (MPV) of the Landau component is quoted as the collected charge at a certain position in the track and the uncertainty is given by the statistical uncertainty from the fit. Examples of performed fits through signal distributions are shown in Figure 8.8. In the plots a value for the χ^2_{red} is given as a measure of the quality of the fit. This value is defined as [49]

$$\chi^2_{red} = \frac{\chi^2}{\text{dof}},$$

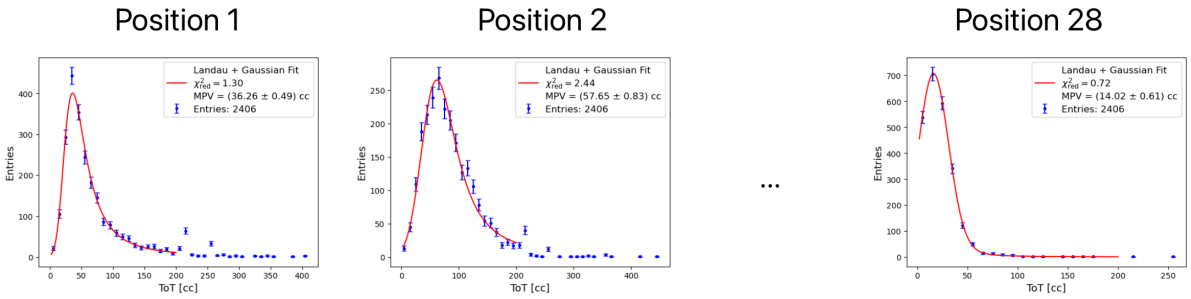

Figure 8.8: Signal distributions (blue) at various positions along downgoing track with track length 28. Each distribution is fitted with a Landau-Gaussian convolution (red). The MPV of the Landau component of the fit is used to represent the collected charge at that location.

where dof stands for degrees of freedom and is equal to the number of data points minus the number of fitted parameters, and χ^2 is defined as

$$\chi^2 = \sum_i \left(\frac{O_i - C_i}{\sigma_i} \right)^2,$$

with O_i the measured data points through which the fit is performed and C_i the values predicted by the fit function. σ_i are the uncertainties on the observed data points. A χ^2_{red} value close to one indicates that the fit was performed well. In the final results, the data points constructed from fits with a $\chi^2_{red} > 3$, will be indicated.

8.2.4 Plots of extracted MPVs

As already discussed, the MPV of the Landau component of the fits through the signal distributions is used to quote the collected charge at a certain position in the track and the uncertainty is given by the uncertainty from the fit. The next step is to collect all these extracted MPVs along with their corresponding uncertainties, in one plot. This plot can be seen as a charge collection profile, showing the ToT in cc as a function of position in units of pixel number in the track. An example of such a plot is shown in Figure 8.9.

8.2.5 Conversion from pixel position to depth

In order to extract information about the charge collection as a function of depth within the sensor, and eventually determine the active thickness of the sensor from this, the x-axis in the charge collection profile generated in the previous step should be converted from position units (pixel number in the track) to the depth in units of µm to which this position corresponds. This conversion can be made by applying trigonometry to the geometrical configuration consisting of the incident particle, the sensor's surface and the sensor's depth, which is schematically represented in Figure 8.10. Applying the cotangent identity from right-angle trigonometry in the triangle denoted in orange yields

$$\cot(\alpha) = \frac{\text{Depth [µm]}}{\text{Position [pixel number]} \times \text{Pitch [µm]}},$$

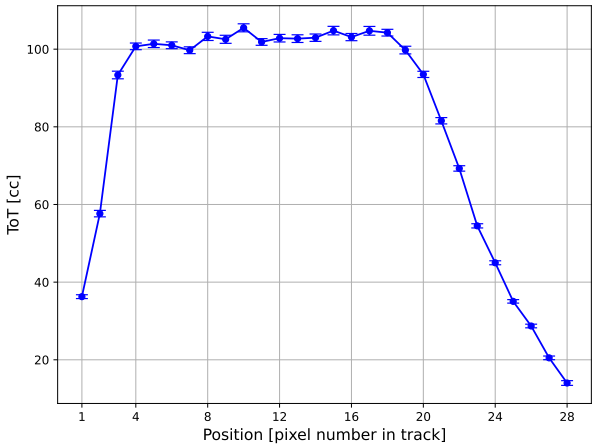

Figure 8.9: Charge collection profile corresponding to data recorded at 89.5° composed of the MPVs of the Landau components of the fits through the signal distributions at different positions along the track.

where α is the rotational angle. The denominator, which is indicated in the sketch by *Position*, is the position in units of pixel number multiplied by the pitch of the DUT in µm to obtain a dimensionless ratio. This formula can now be transformed to a definition of the depth

$$\text{Depth [µm]} = \cot(\alpha) \times \text{Position [pixel number]} \times \text{Pitch [µm]}. \tag{8.1}$$

To perform the conversion, both the pitch of the DUT and the rotational angle α must be known. While the pitch is well-defined and known to be equal to 35 µm, determining the rotational angle α is more challenging. Ideally, this angle could be extracted from the DUT's orientation as determined from the alignment procedure performed by the Corryvreckan software. However, at grazing angles, this approach was found to be unfeasible due to the deteriorated track resolution when the track is projected onto the rotated H2M[1]. Therefore, an alternative method is employed: the rotational angle is estimated based on the charge generated along the particle track, as described in [37]. Figure 8.11 (a) demonstrates the principle of the method. The smaller the incident angle of the particle track, the more silicon will be traversed by the particle and thus the more charge carriers will be generated and eventually collected. Thus the amount of collected charge can be used as a proxy for the amount of silicon traversed by the incident particle. The rotational angle α can be determined by comparing the amount of charge collected whenever the particle is impinging the sensor orthogonally ($\alpha = 0°$), denoted as Q_{ort}, with the amount of charge collected whenever the particle is impinging the sensor under a certain angle, denoted as Q_{tot}. Figure 8.11 shows the geometrical configuration formed by the trajectories of the particles impinging the sensor orthogonally (yellow) and under a certain angle (orange). Applying the sine identity from right-angle trigonometry in the triangle formed by both tracks, yields

$$\cos(\alpha) = \frac{Q_{\text{ort}}}{Q_{\text{tot}}} \iff \alpha = \arccos\left(\frac{Q_{\text{ort}}}{Q_{\text{tot}}}\right). \tag{8.2}$$

[1]Defining the rotational angles based on the alignment procedure would, in fact, necessitate modifications to the current analysis approach.

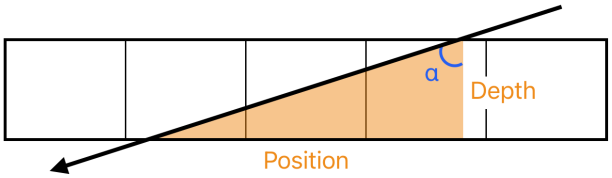

Figure 8.10: Schematic illustration of the geometry underlying the conversion from pixel position to depth in µm (Equation (8.1)).

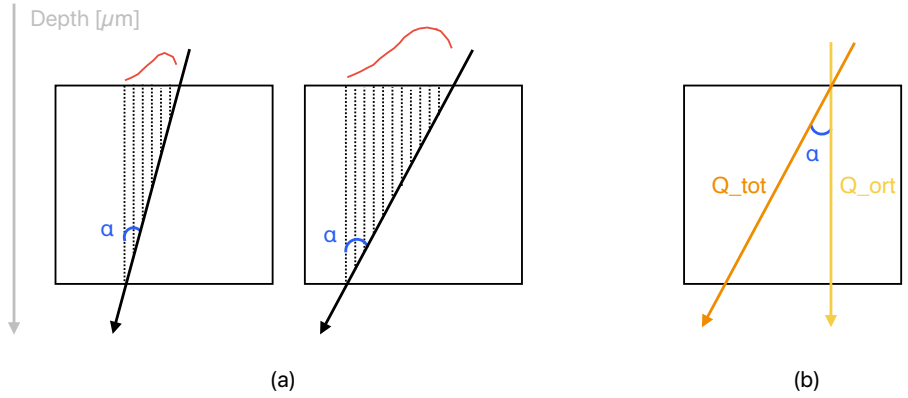

Figure 8.11: Schematic illustration of the principle used to determine the rotational angle α from the charge released along a track (a), and the geometry underlying Equation (8.2).

Thus, in order to determine α one needs to know Q_{ort} and Q_{tot}.

As mentioned in the first section of this chapter, the `[Clustering4D]` module of Corryvreckan provides histograms showing the distribution of charge released by traversing particles, referred to as the cluster charge histograms. To extract the value of Q_{ort}, the cluster charge histogram is fitted with a Landau distribution convoluted with a Gaussian. The reported Q_{ort} corresponds to the MPV of the Landau component, and the associated uncertainty is obtained from the fit. An example of such a cluster charge histogram, along with its corresponding fit, is shown in Figure 8.12a, where both the MPV and its uncertainty are indicated. Also visible in this histogram are two additional bumps one around 212 cc and another one around 256 cc. The events occurring at the location of the second bump (around 212 cc) correspond to events with a ToT value higher than 256 cc, which is the maximum measurable ToT value with an 8-bit DAC. One of such events is illustrated in Figure 8.13. Ones a trigger arrives from the trigger plane, data taking will start in the DUT. The amount of time this data taking takes place is fixed, as denoted in green in the illustration. For events with a ToT value exceeding 256 cc, the signal will not return to baseline within the fixed amount of time available for data taking. As a result, rather than measuring the actual ToT value, the signal is cut-off before decreasing below the threshold value; resulting in the measurement of a cut-off ToT value which is lower than the actual ToT value. As the signal curve of all events featured by a high ToT

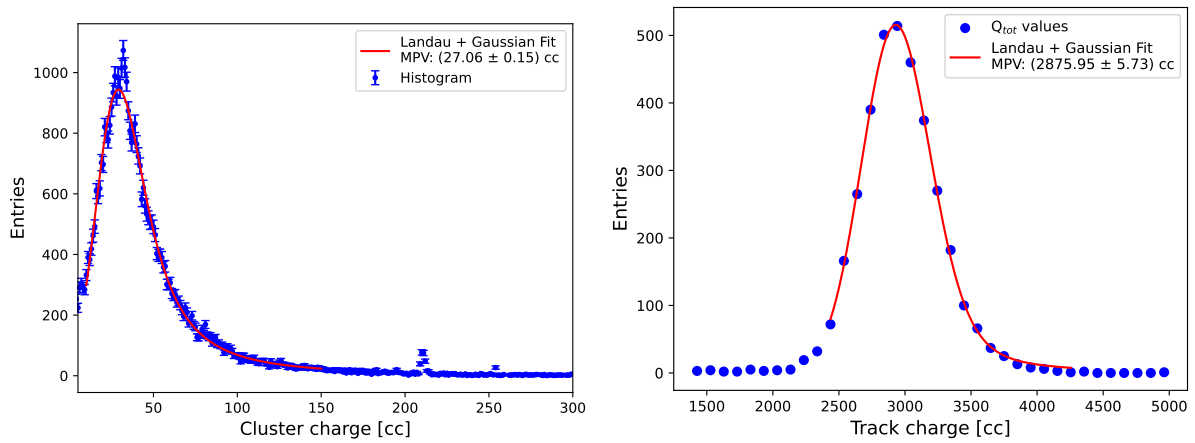

(a) (b)

Figure 8.12: Cluster charge (a) and track charge (b) distribution along with corresponding fit for the determination of Q_{ort} and Q_{tot}, respectively.

value look similar, the same cut-off ToT value of about 212 cc will be measured for all these events; causing a bump in the cluster charge distribution around this value. The other bump, appearing at a ToT value of 256 cc, is related to noisy events, which take place right after the trigger arrived and then saturating the counter. The fit range is chosen to exclude these features.

The determination of Q_{tot} follows a similar procedure, but uses data taken at grazing angles and selects only events with a specific track length. In this case, the relevant histogram displays the total charge released in multiple pixels along the full track of the particle. The total charge per event, referred to as the track charge, is calculated by summing all ToT values recorded for a single particle crossing. This summed value is used to build the track charge histogram, which is then fitted with a Landau distribution convoluted with a Gaussian to extract Q_{tot}. As with Q_{ort}, the quoted value is the MPV of the Landau component. An example track charge histogram and corresponding fit for events with track length 28 is shown in Figure 8.12b, with the extracted Q_{tot} and its uncertainty provided in the plot. To improve the performance of the fit, the data in the histograms was binned.

The found values for Q_{ort} and Q_{tot} can be used in Formula (8.2) to determine the rotational angle α which can then be used in Formula (8.1) to perform the scale conversion from position units to depth units in the charge collection profile shown in Figure 8.9. The result is shown in Figure 8.14a. The uncertainty plotted on the ToT values is the statistical one from the fits through the signal distributions. No uncertainty is quoted on the depth values; however, certain considerations should be taken into account in this context. First of all, the charge collection profile, as presented in Figure 8.14a, represents the obtained average charge collected in the depth layers defined by the sampling of the sensor's depth. These binned measurements across depth intervals can be represented more clearly by explicitly showing the different depth intervals, as can be seen in Figure 8.14b. The width of the bins are defined by the sampling of the depth. For example, the total depth sampled in the example plot is about 9 µm, which is sampled by 28 data points (since only tracks of length 28 are considered). So the bin width is

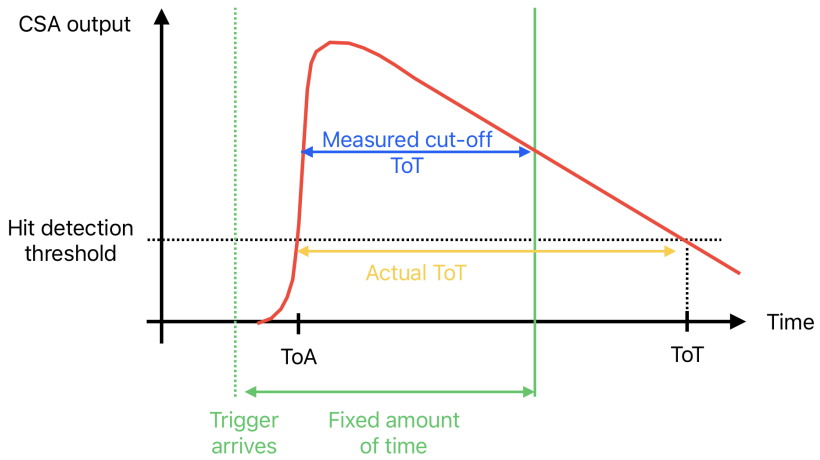

Figure 8.13: Illustration showing the origin of the bump around 212 cc in the cluster charge distribution (Figure 8.12a). The events contributing to this bump are characterized by high ToT values exceeding 256 cc, which are recorded with a cut-off value of approximately 212 cc.

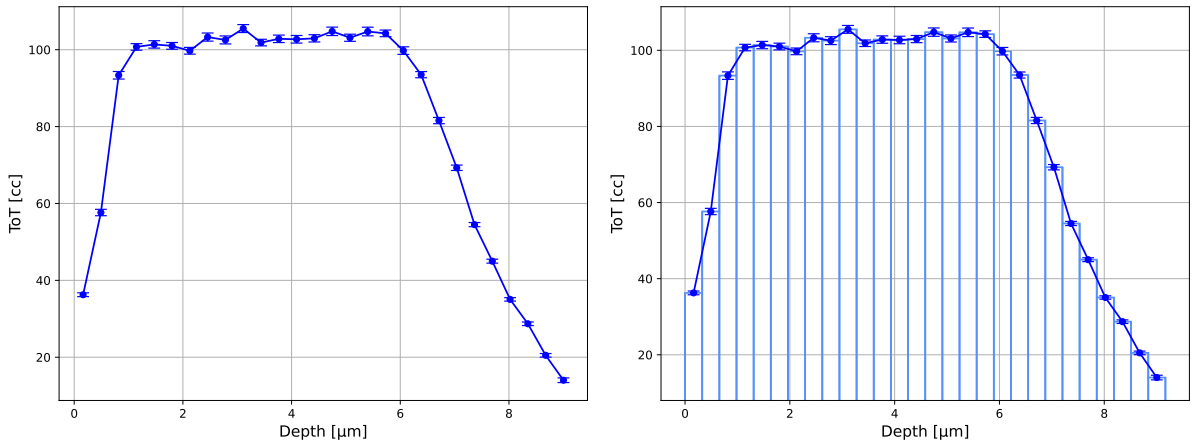

(a) (b)

Figure 8.14: Scaled charge collection profile as a graph (a) and histogram (b), both corresponding to events recorded at 89.5° and exhibiting a track length of 28 pixels.

about 0.3 µm. Rather than considering the effect of the performed binned measurements as an uncertainty on the plotted depth value, the shown data points should be viewed as an average over a certain depth range. For visual simplification, the charge collection profiles will always be shown as the one represented in Figure 8.14a instead of Figure 8.14b. Another source of uncertainty related to the depth arises from the fits performed to determine Q_{ort} and Q_{tot} to calculate the rotational angle α. This statistical uncertainty has been estimated by propagating the uncertainties on Q_{ort} and Q_{tot}, defined by the fit, though Formula (8.2) to get an error on α. Then this error is further propagated through Formula 8.1, where no uncertainties on the position and pitch are considered, to finally get an uncertainty on the depth. This uncertainty is correlated to the depth value and was found to be no higher than 0.05 µm.
Finally, a remark has to be made about the applied method for the scale conversion in the charge collection profiles. Here the amount of collected charge was used as a proxy for the distance traversed by the particle in the silicon. However, as discussed in Section 3.1, the amount of charge released per unit track length depends on the total distance traversed by the particle, even after normalization to the total track length. This introduces a systematic uncertainty, which is not accounted for in the current analysis.

The total active thickness of the sensor is defined as the depth difference between the first and last data points of the charge collection profile.

8.2.6 Applying ToT calibration

A threshold and ToT calibration, obtained from radiation source and test pulse measurements on a per-pixel basis, was applied to the data analysed in this work using the Corryvreckan software. This was done by supplying the calibration file to the `calibration_path_tot` parameter of the `[EventLoaderEUDAQ2]` module corresponding to H2M. As a result, the hits shown in the EventDisplay histograms are converted from ToT in units of clock cycles (cc) to collected charge in units of electrons (e^-). This change of units is propagated through the reconstruction chain and is reflected in the charge collection profiles, where the collected charge at a certain depth is now shown in electrons.

In contrast to the conversion from position in units of pixel number to depth in µm for the x-axis, the ToT calibration does not result in just a scaling of the y-axis due to non-linear response of the front-end. The values along the y-direction are generated though the performance of fits though the signal distributions, as explained in Section 8.2.3. Converting the ToT values in these distributions to charge in electrons, will change the shape of the distribution, and thus also the extracted MPV of the Landau component of the fit through it. The signal distributions are not the only ones affected by the calibration, also the shapes of the cluster charge and track charge distributions, used to extract the Q_{ort} and Q_{tot} values for the determination of α, change. Therefore, applying ToT calibration does not only affect the y-axis, but also the x-axis. The effect of ToT calibration on the signal distributions can be seen in Figure 8.15 where the signal distributions of pixel 15 along the track are shown before (a) and after (b) ToT calibration. After calibration, the signal distribution more closely resembles a Landau distribution, as expected. The ToT calibration corrects for pixel-to-pixel variations, bringing the measured distribution closer to the true energy loss distribution following a Landau shape. The ToT calibrated cluster charge and track charge distributions are shown in Figure 8.16. A comparison between

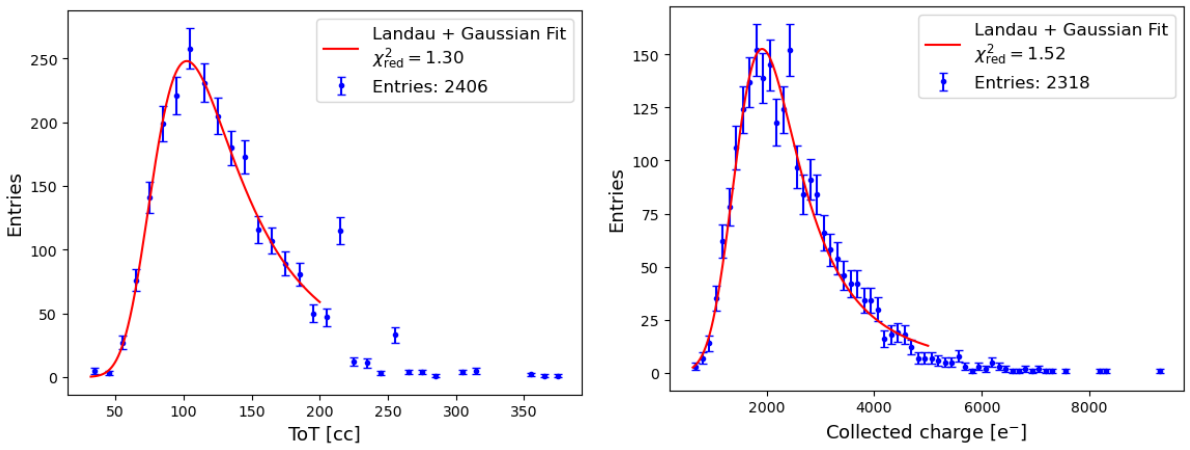

(a) (b)

Figure 8.15: Signal distribution for pixel 15 along the track, before (a) and after (b) ToT calibration.

Figure 8.16a and Figure 8.12a demonstrates an improved fit, more accurately capturing the peak value of the distribution. The resulting charge collection profile is shown in Figure 8.17.

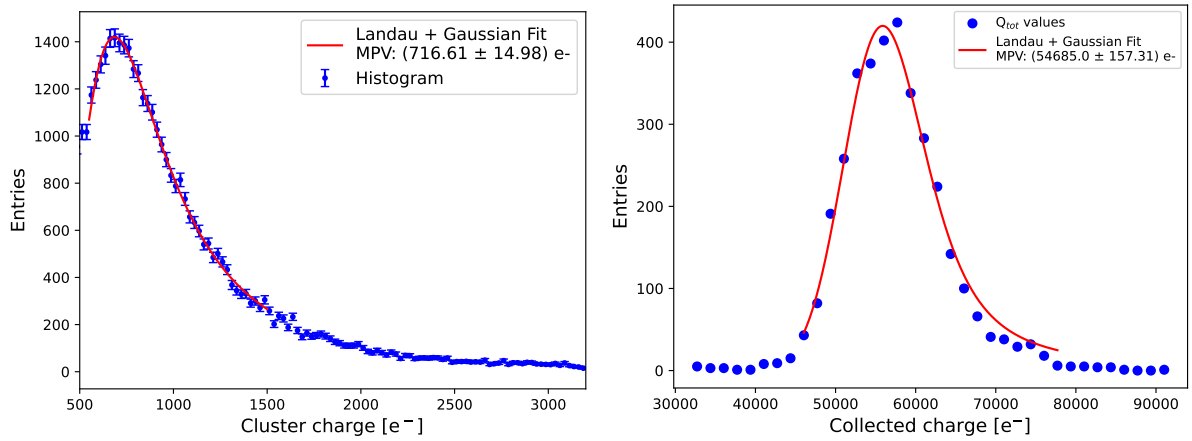

(a) (b)

Figure 8.16: ToT calibrated cluster charge (a) and track charge (b) distributions along with corresponding fit for the determination of Q_{ort} and Q_{tot}, respectively.

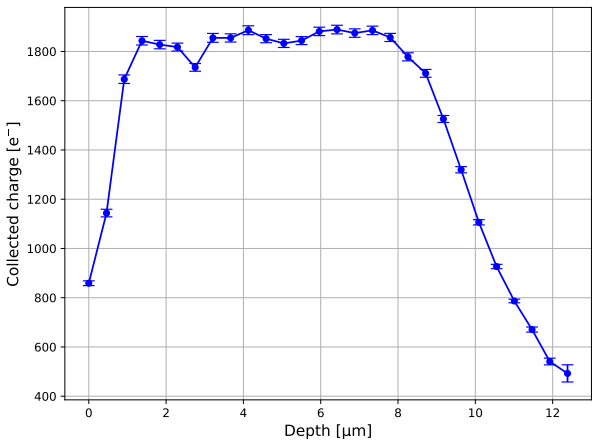

Figure 8.17: Threshold and ToT calibrated charge collection profile.

9. Results

This chapter discusses the results of the analysis, conducted using the methodology outlined in the previous chapter, applied to the various sets of collected data.

9.1 Impact of track lengths

After clustering, the data is segmented according to the event track length. The number of events within multiple track length categories is found to be sufficient to conduct the analysis. To assess the effect of track length on the analysis outcome, the analysis is performed on multiple subsets of the data, each characterized by a different track length, and the results are compared.

The outcomes are shown in Figure 9.1, where the charge collection profiles for various track lengths are presented in units of clock cycles (a) and electrons (b). These results are based on data from dataset 2, recorded at a rotational angle of 89°. The hollow markers denote data points corresponding to poorly fitted signal distributions, defined as those with a reduced chi-squared value (χ^2_{red}) greater than 3. In the right plot, two outliers can be identified near the end. Visual inspection of the signal distribution fits corresponding to these points revealed that the rising edge of the distributions contained relatively few data points. This scarcity led to fits with an unexpected shape and an abnormally low MPV of the Landau component, though characterised by a reduced chi-squared value lower than 3 and thus not indicated by hollow markers in the charge collection profile. Aside from these outliers, both charge collection profiles show good agreement among the curves corresponding to different track lengths. The only difference between the various curves is the number of data points they contain, and thus the precision with which the depth is sampled.

It can therefore be concluded that the results of the analysis are largely independent of the selected track length.

9.2 Charge collection profile regions

The charge collection profiles can be divided into three distinct regions, as illustrated in Figure 9.2. In the first region on the left (blue), charge collection appears incomplete compared to the second region (yellow), where a uniform amount of charge is collected. In the third region (red), the amount of collected charge decreases with depth.

The physical interpretation behind these regions becomes clearer when the charge collection profile is compared with the cross-sectional illustration of H2M, shown in Figure 9.3. To facil-

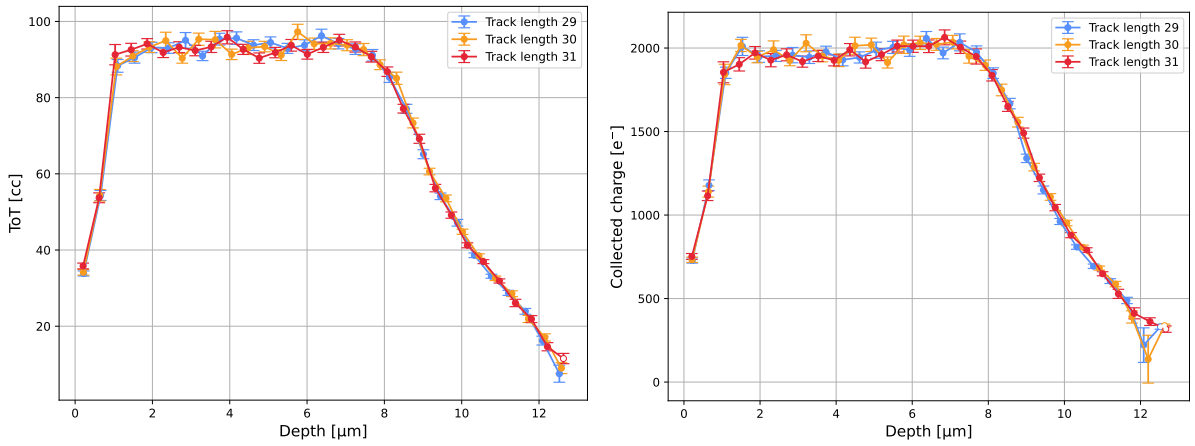

(a) (b)

Figure 9.1: Charge collection profiles in clock cycles (a) and electrons (b) from data subsets with varying track lengths. Analysed data is from dataset 2, taken at 89° rotational angle, a sensor bias voltage of −1.2 V and a hit detection threshold corresponding to approximately 300 e^-. Hollow markers denote data points for which the signal distribution was poorly fitted.

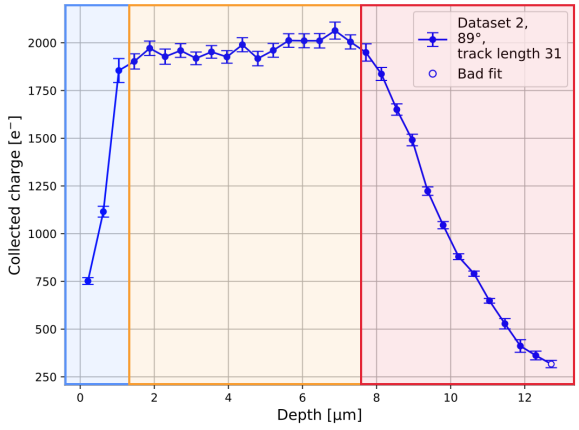

Figure 9.2: The different regions in the charge collection profile, from left to right: region of incomplete charge collection (blue), plateau where the amount of collected charge is constant (yellow), and a decrease of collected charge (red). Data acquired from H2M-8 operated at a sensor bias voltage of −1.2 V and hit detection threshold corresponding to 300 e^-.

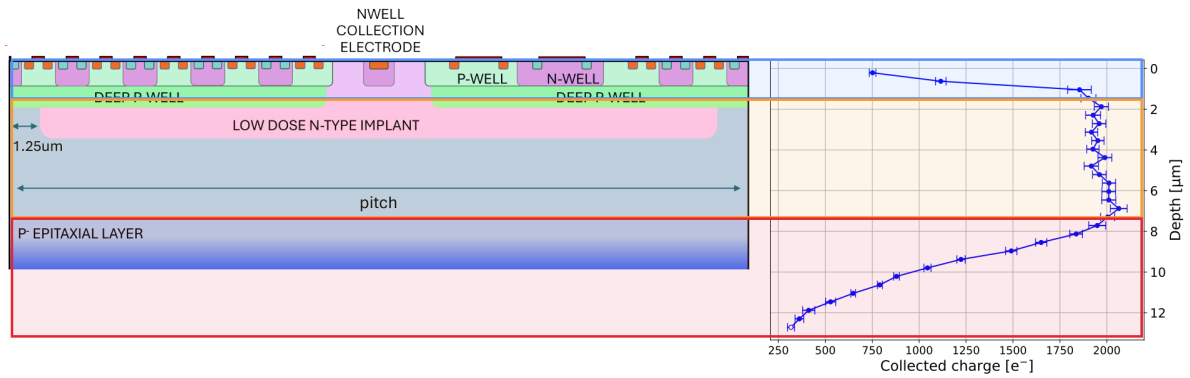

Figure 9.3: Cross-sectional illustration of active area of H2M, modified from [34], and rotated charge collection profile, providing physical interpretation of the three distinguished regions in the charge collection profiles: incomplete charge collection due to the presence of the pixel architecture hosting the transistors (blue), uniform collection in the depleted epitaxial region (yellow), and diffusion in the boundary between the epitaxial layer and high doped substrate (red). The illustration is not to scale and serves only to indicate the approximate correspondence between charge collection layers and sensor regions.

itate comparison, the charge collection profile has been rotated. Since downgoing events have been selected to create this profile, a depth of 0 µm corresponds to the sensor's surface, therefore the origin of the y-axis is placed at the top. The charge collection behaviour in the distinct regions can be assigned to the presence of chip structures at certain depths.

1. The incomplete charge collection in the first region is due to the presence of the deep p-wells hosting the CMOS electronics at the surface of the sensor.
2. The second region is aligned with the epitaxial layer. The uniform collection of charge in this region suggests that this part of the epitaxial layer is depleted. In the following, this region will be referred to as the *depleted region*.
3. The third region, featured by a decreasing amount of collected charge with depth, aligns with the transition region between the epitaxial layer and substrate. This part of the charge collection profile thus corresponds to an undepleted region in the sensor; meaning that at these depths the carrier transport is dominated by the diffusion mechanism. In the following, this region will be referred to as the *diffusion region*.

The following two subsections provide a more detailed discussion of the depleted and diffusion regions in the charge collection profiles. They also present a methodology for objectively quantifying the extent of the various regions.

9.2.1 The depleted region

The depleted region of the sensor is characterized by uniform charge collection, which appears as a plateau in the charge collection profile. Determining the extent of this region therefore comes down to identifying the width of the plateau. In this work, the width is quantified by analysing the first derivative of the charge collection profile, which represents the rate of change in collected charge q with depth z. Within the depleted region, the charge remains approximately

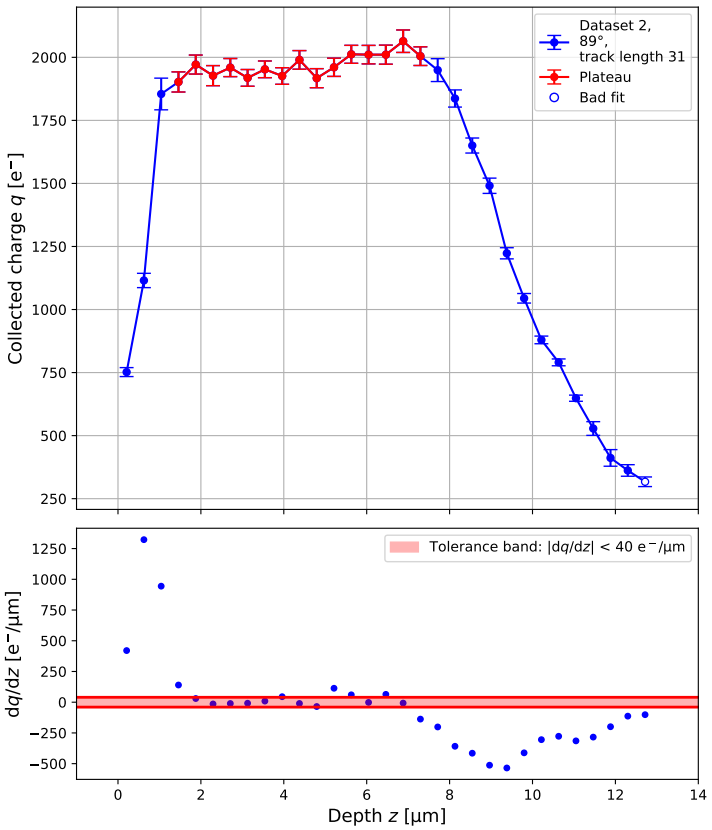

Figure 9.4: Determination of the extent of the depleted region in the charge collection profiles by means of the derivative of the profile. Presented profile is constructed from data acquired from H2M-8 operated at a sensor bias voltage of $-1.2\,\mathrm{V}$ and a hit detection threshold corresponding to approximately $300\,\mathrm{e}^-$.

constant with depth, resulting in a near-zero first derivative. By computing the derivative and identifying the region where its values lie within a small interval around zero, the plateau—and thus the depleted region—can be delineated.

Data points with a corresponding derivative ($\mathrm{d}q/\mathrm{d}z$) within a defined tolerance around zero are assigned to the depleted region. The width of the depleted region is then taken as the distance between the first and last such points. Figure 9.4 shows both the charge collection profile (top) and corresponding derivative values (bottom). The allowed tolerance band around zero is indicated in red in the lower plot. A threshold value of $40\,\mathrm{e}^-\,\mu\mathrm{m}^{-1}$ has been identified to include the data points in the middle of the plateau which can be visually determined from the charge collection profile. As can be seen in the lower plot, some points in the middle of the plateau have derivative values exceeding the tolerated band edges. To also include these points in the depleted region, not only the points with a derivative value within the allowance band, but also the points next to these points are included in the depleted region. As a result, the depleted region is also extended by one data point to the left and right. The final identified depleted region is indicated in red in the plot at the top. Again, the hollow markers denote the data

points corresponding to signal distributions with a poorly performed fit. The exact threshold value used to construct the tolerance band is increased for charge collection profiles that exhibit visually higher fluctuations within the depleted region, or decreased when non-calibrated charge collection profiles are analysed. However, the underlying principle remains unchanged. In some charge collection profiles, the final points in the diffusion region show only minor variation in charge collection with depth, which may lead to their incorrect assignment to the depleted region. In such cases, the affected points are manually excluded.

As the depleted region separates the first and last region, the determination of its extent comes with the determination of the extent of the other two regions. The first region consists of data points preceding the depleted region, while the data points that follow correspond to the diffusion region. The extent of these regions is given by the depth difference between the last and first data points in the corresponding region. For the example shown in Figure 9.4, 5.8 µm of the total active thickness of 12.5 µm is assigned to the depleted region. The extent of the first region is 1.3 µm and the diffusion region is 5.4 µm.

9.2.2 The diffusion region

For charge carriers generated outside the depleted region, diffusion is the dominant transport mechanism as described in Section 3.2.3. In this region — referred to as the diffusion region — the number of carriers reaching the electrode, and thus contributing to the signal, decreases with depth due to the increased probability of recombination at greater distances from the collection site. In [26] an expression is provided for the induced charge q measured at the collection electrode as a function of the depth x_0 at which the charge is generated. This expression was found by solving Equation (3.2) from Section 3.2.3, i.e. determining an expression for the number density of excess minority carriers (electrons), $n(x,t)$, as a function of time t and depth x [50]. Using Formula (3.1) from Seciton 3.2.3, an expression for the current $\vec{j}_{n,diff}$ entering the depletion region could be determined. Finally, this current is converted into an induced charge measured at the electrode, by assuming that all carriers entering the depletion layer are totally collected and integrating over time. Assuming the integration time of the electronic readout chain significantly exceeds the carrier lifetime, the expression for the induced charge q measured at the collection electrode as a function of the depth x_0 at which the charge is generated, was found to be an exponentially decaying function, as described in [26]

$$q(x_0) = N \exp\left(-\frac{x_0 - w}{L_n}\right),$$

where N is the number of electron-hole pairs generated by a single particle at a depth x_0, L is the electron diffusion length, and w is the depletion layer depth. Fitting this function to the charge collection profiles provides a way to determine the diffusion length. Applying the fit only to the diffusion region of the charge collection profile allows to omit the w parameter, simplifying the fit. The utilized fit function has the form

$$y(x) = a \exp\left(b \times x\right), \tag{9.1}$$

with $y(x)$ the amount of collected charge in electrons and x the depth in µm. Fit parameter a corresponds to a scaling factor, and the diffusion length L_n is determinable from fit parameter b as $b = -1/L_n$. This methodology has been applied to both data acquired from H2M-2 and

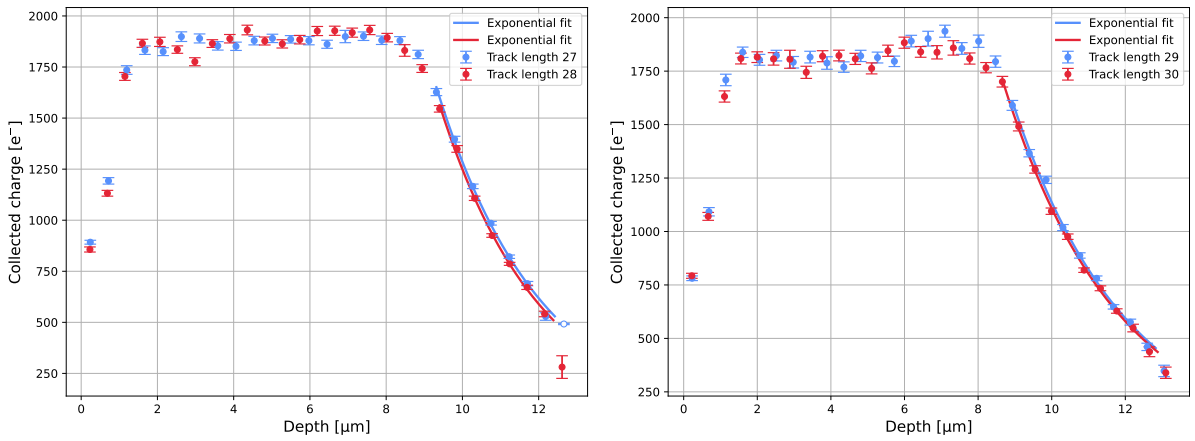

(a) (b)

Figure 9.5: Exponential fits of the form given in Formula (9.1) applied to the diffusion regions of the charge collection profiles for H2M-2 oriented at 89.5° (a) and H2M-8 oriented at 89° (b), both operated at a sensor bias voltage of $-3.6\,\mathrm{V}$ and hit detection threshold corresponding to $300\,\mathrm{e}^-$. Physical quantities derived from fit parameter b are listed in Table 9.1.

H2M-8 as shown in Figure 9.5. To both chips, H2M-2 and H2M-8, oriented at 89.5° and 89°, respectively, a sensor bias voltage of $-3.6\,\mathrm{V}$ was applied and a threshold setting of approximately $300\,e^-$ was employed. For both chips, data of two track lengths is investigated. The exponential fit is applied to a subset of datapoints within the diffusion region. Specifically, points at the beginning, where the transition from the depleted to the diffusion region occurs, and those at the end, affected by poorly fitted signal distributions, are excluded. The obtained values for the diffusion length L_n derived from fit parameter b are shown in Table 9.1. Making use of Equation (3.3) the found results for the diffusion length can be converted into carrier lifetimes. For the diffusion coefficient D_n a value of $3.6\,\mu\mathrm{m}^2\,\mathrm{ns}^{-1}$ is used [24]. It should be noted that the diffusion coefficient depends on the carrier mobility, which in turn varies with the doping concentration [24]. Since the diffusion region likely spans the transition between the epitaxial layer and the highly doped substrate, the doping concentration is expected to change over the fitted range of the charge collection profile. Nevertheless, in this analysis, a constant diffusion coefficient is assumed across the entire region. The resulting carrier lifetimes can also be found in Table 9.1.

Almost all obtained values are consistent within three times the quoted fit uncertainties, confirming that the analysis is independent of the selected track length and indicating that the thinning procedure does not affect the sensor's properties in the active layer. It is also worth noting that the determined carrier lifetimes are significantly shorter than the integration time of the electronic readout chain (which is about 10 ms for H2M while operated in ToT mode), validating the earlier assumption leading to the used expression for the exponential fits.

Table 9.1: Summary of physical quantities derived from fit parameter b obtained from applying exponential fits (Formula (9.1)) to the diffusion region of the charge collection profiles for H2M-2 and H2M-8, shown in Figure 9.5. Quoted uncertainties are the propagated statistical uncertainties obtained from the fit.

Chip sample	**Diffusion length L_n from fit parameter b**	**Carrier lifetime τ_n**
H2M-2	(2.7 ± 0.1) µm (2.7 ± 0.1) µm	(2.1 ± 0.1) ns (2.0 ± 0.1) ns
H2M-8	(3.1 ± 0.1) µm (3.1 ± 0.1) µm	(2.6 ± 0.1) ns (2.7 ± 0.1) ns

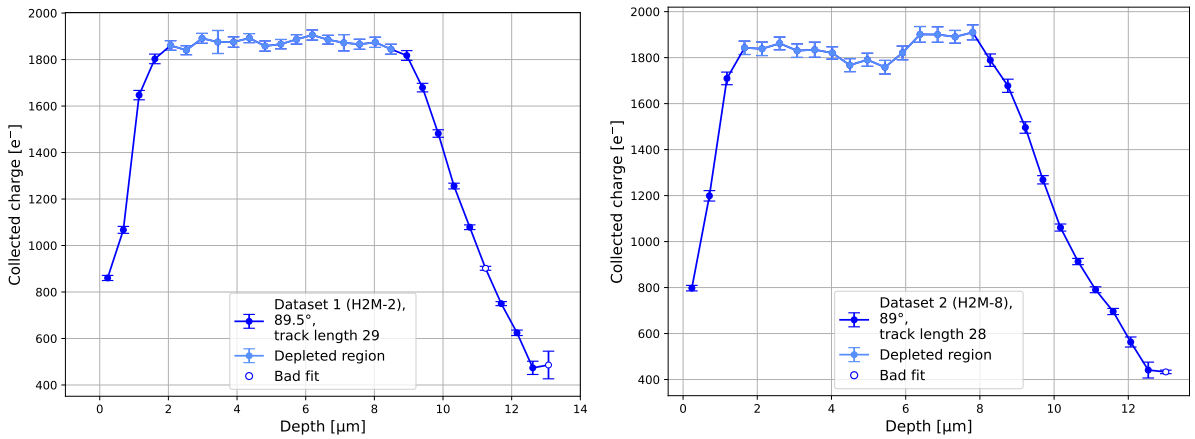

(a) (b)

Figure 9.6: Charge collection profiles for samples with different total chip thickness: (a) H2M-2 with a chip thickness of 50 µm and an active thickness of about 12.8 µm and (b) H2M-8 with a chip thickness of 25 µm and an active thickness of about 12.8 µm. Both chips are operated at a sensor bias voltage of -3.6 V and hit detection threshold corresponding to 300 e^-.

9.3 Impact of backside thinning on the active thickness

As already discussed in Chapter 7 in both test beams of which the data are presented in this work, a different H2M sample was employed. The total chip thickness of sample H2M-2, from which the data in dataset 1 originate, is 50 µm, whereas the data of dataset 2 originate from sample H2M-8 with reduced total thickness of 25 µm. Comparing the results from both datasets where the chip was operated under the same conditions (applied sensor bias voltage of -3.6 V and hit detection threshold corresponding to 300 e^-), makes it possible to investigate the effect of sample thinning on the active thickness of the sensor. The results are shown in Figure 9.6.

The found value for the total active thickness of H2M-2 is about 12.8 µm, of which 1.8 µm is assigned to first region, 6.4 µm to the depleted region and 4.6 µm to the diffusion region. For H2M-8 a total active thickness of about 12.8 µm is found as well, with 1.4 µm in the first region, 6.2 µm in the depleted region and 5.2 µm in the diffusion region. It can therefore be concluded

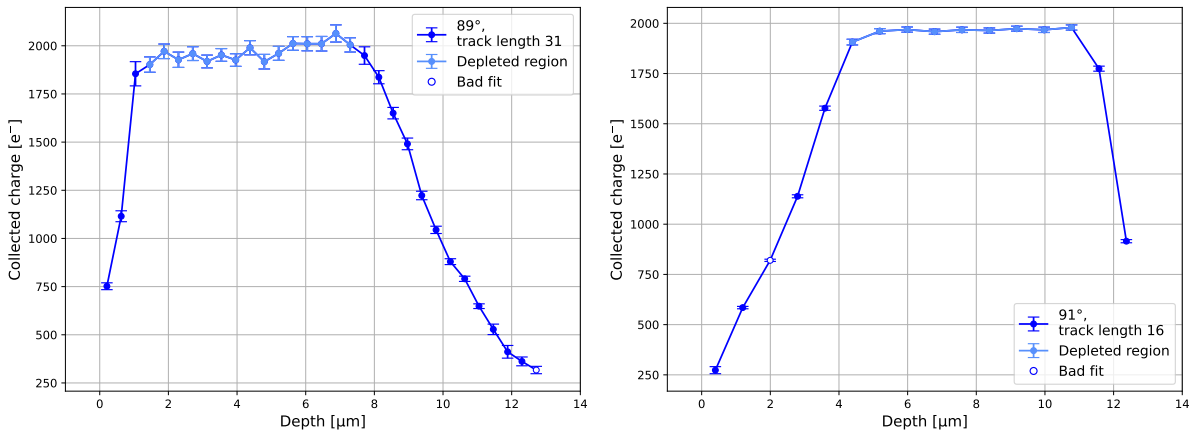

(a) (b)

Figure 9.7: Charge collection profiles for two different chip (H2M-8) orientations: (a) chip oriented at a rotational angle of 89°, beam particles enter the sensor from the sensor surface (b) chip oriented at a rotational angle of 91°, beam particles enter the sensor from the sensor backside. For both orientations the chip was operated under the same sensor bias voltage ($-1.2\,\mathrm{V}$) and hit detection threshold ($300\,\mathrm{e}^-$).

that backside thinning to 25 µm has no significant effect on the active thickness of the H2M, which is consistent with expectations—given that the active region is approximately 10 µm thick and located in the upper half of the sensor.

9.4 Impact of chip parameters on active thickness

9.4.1 Chip orientation

By changing the orientation of the chip in the test beam setup, it is possible to investigate the difference between charge collection depending on whether a beam particle enters the sensor from the surface or backside. For this purpose, the data acquired from H2M-8 conducted at rotational angles of 89° and 91° are compared. Figure 9.7 presents the results: the charge collection profile from data acquired at 89° is shown on the left, while the profile from 91° data is shown on the right. A comparison of the two charge collection profiles suggests that one is a mirror image of the other with respect to the y-axis, as expected. Namely, in the 89° configuration, beam particles enter the sensor from the sensor's surface, traversing first the depletion layer and then the diffusion region. On the other hand, when the chip is oriented at 91°, the particles follow the reverse path—starting in the diffusion region and exiting through the surface. The overall shape and symmetry between the profiles shown in Figure 9.7 is therefore expected from the reversed order in which the sensor depth is sampled in both configurations.

To verify the assumption of one of the profiles being a mirror image of the other profile, one of them can be reflected across the y-axis and both can be drawn in the same plot for convenient comparison. The result is shown in Figure 9.8, where the indications of poorly fitted distributions and depleted region points have been omitted for clarity. As can be seen in this figure,

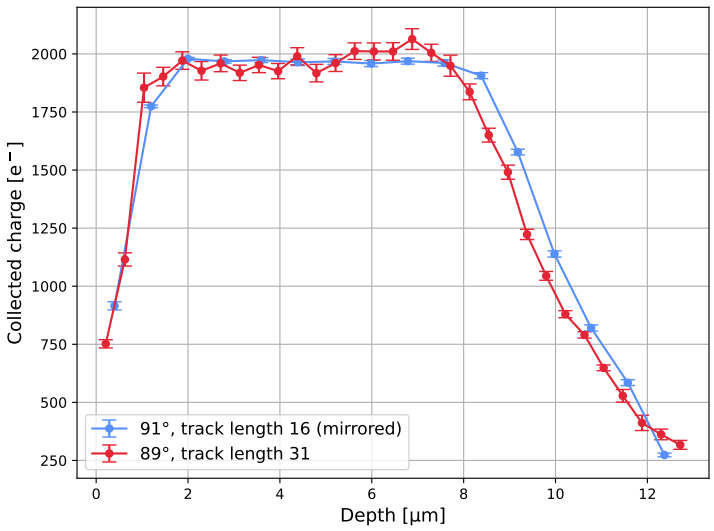

Figure 9.8: Charge collection profiles measured with the sensor oriented at 89° (red) and 91° (blue). For ease of comparison, the profile obtained at 91° has been mirrored across the y-axis to highlight the expected symmetry between the two configurations.

both curves exhibit a strong degree of overlap, suggesting one is indeed the mirror image of the other. The overlap along the y-direction also indicates that the amount of collected charge is the same in both configurations. The overlap along the x-direction can also be verified quantitatively by comparing the extracted values for the total active thickness and the extent of the different regions in the profiles. The values found for the total active thickness are 12.0 µm at 91° and 12.5 µm at 89°. These two results are consistent with each other once the difference in sampling resolution is taken into account. For the dataset taken at 91°, the most frequently observed track length is 16 pixels. In contrast, the 89° dataset shows one of the highest event counts for a track length of 31 pixels. This difference in the most common track length could arise from slight variations in the actual chip orientation in the test beam, possible meaning that the orientational angle was a bit higher than 91° in reality. This implies that the depth sampling in the 89° data is nearly twice as fine as in the 91° data. Consequently, the histogram bins used to interpret the charge collection profiles represent almost twice the width in the 91° dataset compared to the 89° one. In other words, each data point in the 91° profile corresponds to charge collected over a depth layer that is nearly twice as thick. Taking this difference into account, the total active thicknesses at both orientations can be considered consistent. The values found for the different regions within the charge collection profile are summarized in Table 9.2.

In conclusion, the only difference between the charge collection profiles obtained from beam particles entering the sensor from the surface versus the backside, is the sampling order of the depth. The obtained total active thickness is consistent in both cases, and an equivalent amount of charge is collected.

Table 9.2: Summery of extracted region extents in charge collection profiles corresponding to H2M-8 oriented under two different rotational angles.

Rotational angle	**Total active thickness**	**First region**	**Depleted region**	**Diffusion region**
89°	12.5 µm	1.3 µm	5.8 µm	5.4 µm
91°	12.0 µm	1.6 µm	6.4 µm	4.0 µm

9.4.2 Hit detection threshold

To study how variations in the hit detection threshold—used to compare the detected signal to obtain the ToT value, as explained in Chapter 4—affect the sensor's active thickness, data collected under different threshold settings are analysed. Specifically, for measurements performed at two sensor bias voltages, $-0.8\,\mathrm{V}$ and $-1.2\,\mathrm{V}$, two different threshold levels were applied: one corresponding to approximately $300\,\mathrm{e}^-$ and another one corresponding to approximately $400\,\mathrm{e}^-$. At each sensor bias setting, the effect of the threshold is investigated independently. All data analysed in this section were acquired using H2M-8, oriented at 89°.

Figure 9.9 and Figure 9.10 show the charge collection profiles corresponding to an applied sensor bias of $-0.8\,\mathrm{V}$ and a threshold level corresponding to $300\,\mathrm{e}^-$ and $400\,\mathrm{e}^-$, on the left and right, respectively. The charge collection profiles presented in Figure 9.9 are resulting from data that have not been threshold and ToT calibrated, whereas the ones in Figure 9.10 are calibrated. Comparing Figure 9.10a and Figure 9.10b, the collected charge appears slightly higher at the lower threshold setting, as expected. The active thicknesses corresponding to the profiles shown in Figure 9.9 are 12.6 µm at a threshold of $300\,\mathrm{e}^-$ (left) and 9.9 µm at a threshold of $400\,\mathrm{e}^-$ (right). Thus, this result suggests that increasing the threshold level by about $100\,\mathrm{e}^-$, decreases the active region inside the sensor by almost 3 µm. Although, this variation in active thickness does not reflect an actual physical change, but rather a readout artefact. Namely, increasing the configured threshold level will decrease the overall measured ToT values. This affects the determined $Q_{\mathrm{ort}}/Q_{\mathrm{tot}}$ value. For the data presented in Figure 9.9, this ratio was about 0.013 for the lower threshold setting (left) and 0.010 for the higher threshold setting (right). As this ratio is used to scale the x-axis, as explained in Section 8.2.5, this difference will also have a significant effect on the determined depth. The lower the ratio, the lower the depth will be, as observed in Figure 9.9. The fact that the determined ratios differ between the two measurements, despite being conducted at the same rotational angle α, suggests that the increase in collected charge in ToT units with increasing particle track length in the sensor does not scale consistently across different threshold settings.

This effect can be taken into account by threshold and ToT calibrating the data. The resulting charge collection profiles, after calibration, are shown in Figure 9.10. The active thicknesses corresponding to these profiles are 12.7 µm and 12.6 µm, at lower (left) and higher (right) threshold settings, respectively. The earlier observed variation in active thickness with selected threshold level therefore seems to no longer be present. This observation validates the expectation of the calibration procedure to correct for non-linear electronics responses, such as those due to the threshold setting.

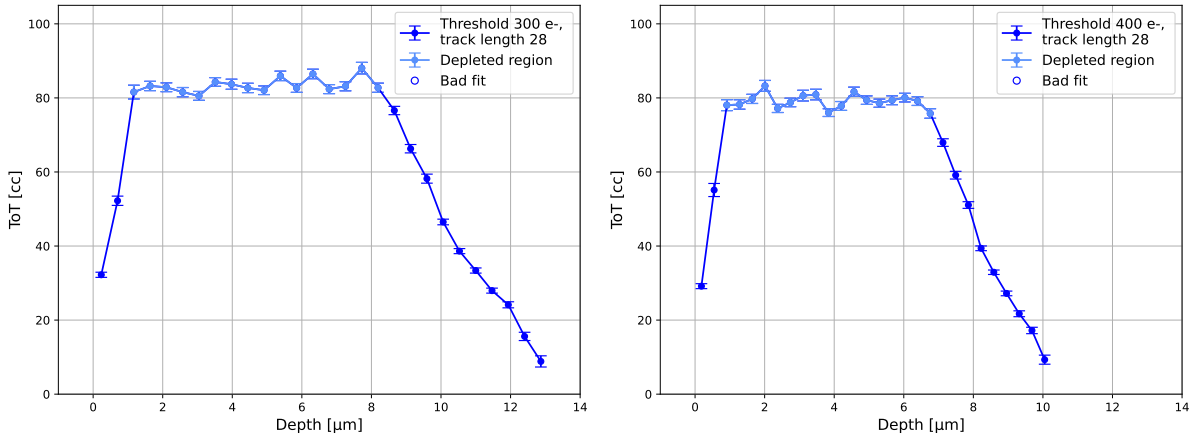

(a) (b)

Figure 9.9: Charge collection profiles for H2M-8 oriented at 89° under a sensor bias voltage of −0.8 V, shown for two different threshold settings: (a) approximately 300 e^- and (b) approximately 400 e^-.

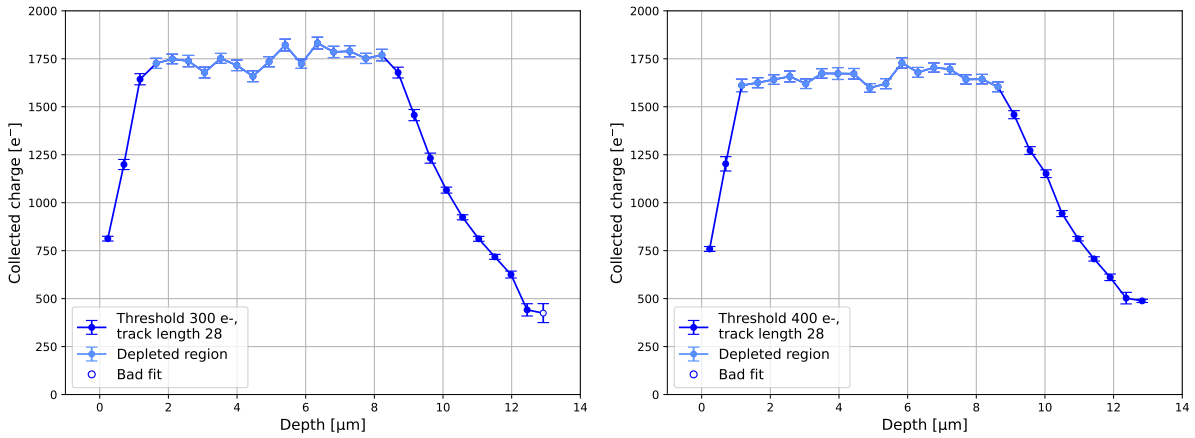

(a) (b)

Figure 9.10: Threshold and ToT calibrated charge collection profiles for H2M-8 oriented at 89° under a sensor bias voltage of −0.8 V, shown for two different threshold settings: (a) approximately 300 e^- and (b) approximately 400 e^-.

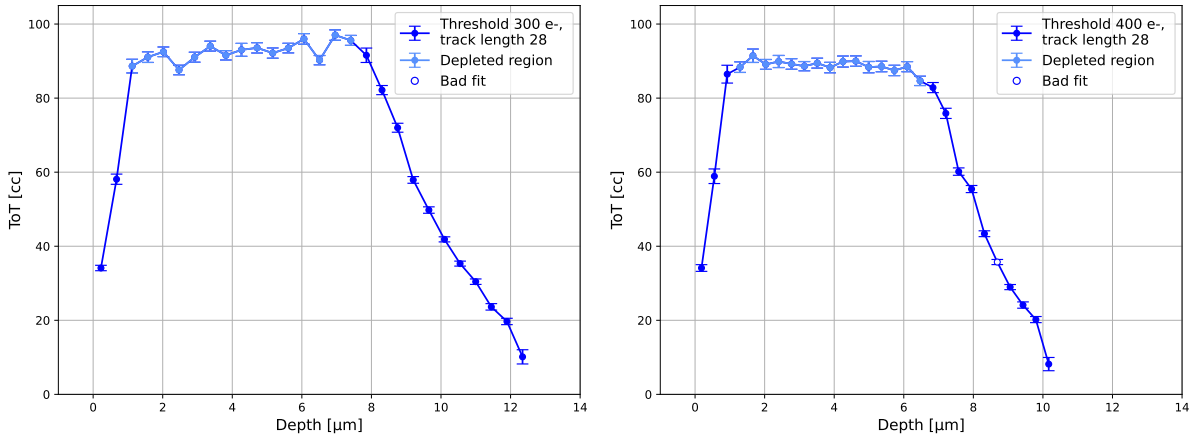

(a) (b)

Figure 9.11: Charge collection profiles for H2M-8 oriented at 89° under a sensor bias voltage of −1.2 V, shown for two different threshold settings: (a) approximately 300 e^- and (b) approximately 400 e^-.

This same behaviour is also observed in the data acquired at an applied sensor bias voltage of −1.2 V, as can be seen in Figure 9.11 (before calibration) and Figure 9.12 (after calibration). Before calibration the determined active thicknesses are 12.1 µm at the lower threshold setting and 10.0 µm at the higher threshold setting. Which are then changed to 12.5 µm and SI12.4 after calibration, respectively.

In conclusion, the active thickness of the sensor remains independent of the selected hit detection threshold level when threshold and ToT calibration is applied and the function of the calibration procedure to correct for non-linear electronics responses has been validated.

9.4.3 Applied sensor bias voltage

Another parameter of which the effect on the determined active thickness can be investigated is the applied sensor bias voltage. To this end, the data acquired using H2M-8, oriented at 89° and operated at a hit detection threshold corresponding to approximately 300 e^- are used. Three different sensor bias voltages were applied to the sensor: −0.8 V, −1.2 V and −3.6 V. The results are shown in Figure 9.13. The active thicknesses conducted from the shown charge collection profiles are 12.7 µm, 12.5 µm and 12.8 µm, corresponding to the data acquired at −0.8 V, −1.2 V and −3.6 V, respectively. These results are consistent when taking into account the width of a sampling layer in the case of an active thickness of about 13 µm and a track length of 28, which is about 0.5 µm. Apart from the total active thickness, also the extent of the depleted region was determined. For this 6.6 µm, 5.8 µm and 6.2 µm were identified at −0.8 V, −1.2 V and −3.6 V, respectively. However, when examining the charge collection profile corresponding to −1.2 V, the width of the depleted region may be underestimated by the method used to determine it. As it visually seems like some points to the right of the defined depleted region might also be part of the depleted region. Therefore, the slightly smaller value found for the depleted region

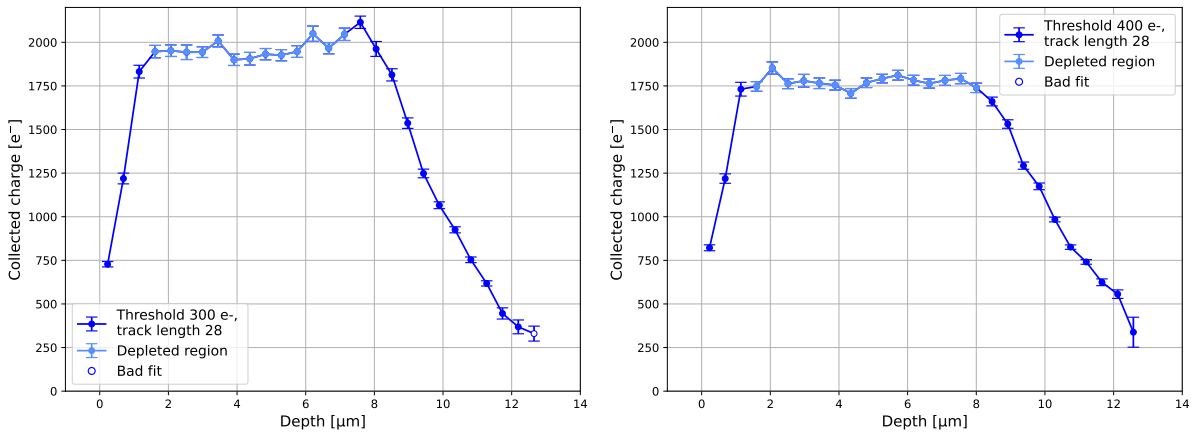

(a) (b)

Figure 9.12: Threshold and ToT calibrated charge collection profiles for H2M-8 oriented at 89° under a sensor bias voltage of −1.2 V, shown for two different threshold settings: (a) approximately 300 e^- and (b) approximately 400 e^-.

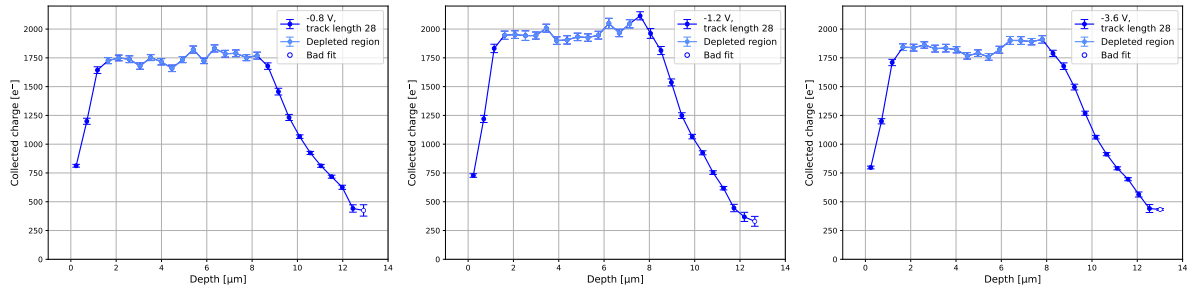

(a) (b) (c)

Figure 9.13: Charge collection profiles for H2M-8 oriented at 89° and operated at a threshold value corresponding to approximately 300 e^- under different sensor bias voltages: (a) −0.8 V (b) −1.2 V and (c) −3.6 V.

at −1.2 V is not considered significant. Another notable difference between the three shown charge collection profiles is their extent in the y-direction. An increase in collected charge is expected with increasing applied sensor bias voltage, as higher voltages accelerate charge collection, reducing the probability of charge loss due to recombination or trapping. While this trend is observed between −0.8 V and −1.2 V, a decrease in collected charge is noted when increasing the voltage further to −3.6 V. This discrepancy is likely related to the calibration procedure, as in the calibrated data the determined value for Q_{tot} is lower in the −3.6 V data than in the −1.2 V data, whereas the expected increase in Q_{tot} with applied bias voltage is observed in the uncalibrated data.

In conclusion, no significant changes in the active thickness of the sensor were observed with varying applied sensor bias voltage.

10. Conclusion

Conducted within the scope of the Tangerine project, in this thesis the active thickness of the H2M chip, a silicon MAPS produced in a novel 65 nm CMOS Imaging Technology with a small collection electrode design, was investigated.

To this end, data from two test beam campaigns were analysed, one conducted in May 2024 and the other one in February 2025. A different H2M sample was employed in both test beam campaigns: the H2M-2 sample, with a total chip thickness of 50 µm was used in May and the H2M-8 sample with reduced chip thickness of 25 µm in February. A notable aspect of the detector configuration used in these test beam campaigns was the orientation of the DUT. Typically, the sensor surface is positioned perpendicular to the particle beam, but in this case, data were also collected with the DUT rotated to an angle of approximately 89°, causing the beam particles to impinge on the sensor at shallow angles. As a result, the particles traversed multiple adjacent pixels, each at a different depth. From this information, the charge collection profiles, displaying the amount of collected charge as a function of the depth inside the sensor, could be constructed. The extent of the profile provided a measure for the active thickness of the sensor, while its shape allowed investigation of charge collection at different depths. This method, in which information about the charge collection as a function of depth inside the sensor is generated through the use of ionizing particles impinging the sensor under shallow angles, is known as the grazing angle method.

The test beam data analysis followed a two-step procedure: first, the data were organized using the Corryvreckan software designed for offline reconstruction and analysis of test beam data; then, this processed data served as input for the second step, which generated the charge collection profiles.

The analysis resulted in several key findings. First of all, it was proven that the grazing angle method works for the H2M chip. The analysis produced charge collection profiles that aligned with the dimensions and shape expected from the sensor design. Overall, a total active thickness of approximately 13 µm, of which ~ 2 µm corresponded to a region with incomplete charge collection due to the presence of the deep p-wells, ~ 6 µm was assigned to the region in the profile where the collection was found to be uniform (depleted region), and the last ~ 5 µm was assigned to the region in which the collected charge exponentially decreased with depth (diffusion region). A deeper investigation of the diffusion region made it possible to determine the electron diffusion length in the corresponding layer of the sensor, from which the carrier lifetime could be determined. A value of (2.1 ± 0.1) ns was found for H2M-2 and of (2.6 ± 0.1) ns for H2M-8. Both are consistent within three times the quoted fit uncertainties, indicating that the backside

thinning procedure by which the thinned sample was manufactured, does not affect the sensor's properties in the active layer. This has also been validated by the determined active thickness for both samples, which was about 12.8 µm for both. The impact of several chip parameters on the active thickness has been investigated as well. Illuminating the sensor from the surface or backside was found to only have an impact on sampling order of the depth. The obtained total active thicknesses were consistent, and an equivalent amount of charge was collected in both configurations. Changing the hit detection threshold was found to have no impact on the total active thickness after threshold and ToT calibration was applied. As this observation was only found after calibration, it also validated the function of the calibration procedure to correct for non-linear electronics responses. Increasing the threshold value was found to decrease the total amount of collected charge, as expected. Lastly, also the impact of changing the applied sensor bias voltage was investigated. No significant changes in the active thickness of the sensor were observed with varying applied sensor bias.

11. Outlook

The determined values for the sensor's active thickness, and its internal regions, can be used as an input for TCAD generic layouts simulating the H2M sensor. The improved knowledge of the sensor layout enables a more accurate representation of the sensor, and thus a more reliable investigation of its properties.

However not explicitly discussed in this thesis, the suggestion of a slight change in charge collection rate with depth in the diffusion region was observed. The physical interpretation of this "bump" is not fully established yet and might require further investigation using TCAD simulations. A possible explanation for the origin of this feature is the presence of a non-totally flat depleted line in between the highly doped substrate and the lower doped epitaxial layer. Additional data, for example acquired from a chip operated in ToA mode, could enable further investigation, from which the charge collection time at different sensor depths could be resolved.

Despite the progress made, there remain aspects of the analysis that could be further refined, for example by taking into account additional relevant effects. One of these effects is the fact that the amount of charge carriers released by an ionizing particle in silicon per unit track length depends on the total track length of the particle through the material, even after normalisation with respect to the total track length. As in the analysis the amount of collected charge is used as a proxy for the track length in the determination of the rotational angle of the DUT, this effect introduces a systematic uncertainty on the depth, which should be taken into account in further analysis.
Finally, a detailed investigation into the depth-related uncertainties should be performed.

Acknowledgments

I would like to express my deepest gratitude towards Ingrid and Simon, for welcoming me in their research groups. I would also like to thank professor Tytgat, for making it possible for me to conduct this project as my master thesis.

I am very grateful for my supervisors at DESY. Thank you Simon, for the opportunity to work on this project, the discussions, support and keyboard ASMR from across the hallway. Thank you Sara, for your support, time, huge amount of patience, answers to all my naive questions, and daily reminders to take a coffee break. I would also like to thank Finn for the insightful discussions, coding assistance, and the excellent apples and cookies during the test beam.

I would like to extend this gratitude to all members of the Tangerine group. Thank you for your valuable comments and suggestions during the weekly meetings.

Thank you to the whole DESY ATLAS group, for the endless Airfryer discussions over lunch and the delicious cakes. And to the ATLAS ITk Interposing team, for all the gluing fun in the cleanroom.

Last but certainly not least, a huge thank you to my friends and family. For your unconditional support, numerous check-ins, updates from home (especially those about the plants in my room and the *Plantentuin*), cute pet pictures and your willingness to listen to me yapping for hours.

Bibliography

[1] J. J. Thomson. "XL. Cathode Rays". In: *The London, Edinburgh, and Dublin Philosophical Magazine and Journal of Science* 44.269 (1897), pp. 293–316. DOI: 10.1080/14786449708621070. eprint: https://doi.org/10.1080/14786449708621070. URL: https://doi.org/10.1080/14786449708621070.

[2] L. Evans and P. Bryant. "LHC Machine". In: *Journal of Instrumentation* 3.08 (Aug. 2008), S08001. DOI: 10.1088/1748-0221/3/08/S08001. URL: https://dx.doi.org/10.1088/1748-0221/3/08/S08001.

[3] The ATLAS Collaboration. "The ATLAS Experiment at the CERN Large Hadron Collider". In: *Journal of Instrumentation* 3.08 (Aug. 2008), S08003. DOI: 10.1088/1748-0221/3/08/S08003. URL: https://dx.doi.org/10.1088/1748-0221/3/08/S08003.

[4] The CMS Collaboration. "The CMS experiment at the CERN LHC". In: *Journal of Instrumentation* 3.08 (Aug. 2008), S08004. DOI: 10.1088/1748-0221/3/08/S08004. URL: https://dx.doi.org/10.1088/1748-0221/3/08/S08004.

[5] *Home — CERN*. May 2025. URL: https://home.cern/.

[6] M. Thomson. *Modern Particle Physics*. Sept. 2013. DOI: 10.1017/cbo9781139525367. URL: https://doi.org/10.1017/cbo9781139525367.

[7] Wikipedia contributors. *File:Standard Model of Elementary Particles.svg - Wikipedia*. Sept. 2019. URL: https://en.m.wikipedia.org/wiki/File:Standard_Model_of_Elementary_Particles.svg.

[8] H. M. Gray. "Future colliders for the high-energy frontier". In: *Reviews in Physics* 6 (2021), p. 100053. ISSN: 2405-4283. DOI: https://doi.org/10.1016/j.revip.2021.100053. URL: https://www.sciencedirect.com/science/article/pii/S2405428321000022.

[9] A. Crivellin and Bruce Mellado. "Anomalies in particle physics and their implications for physics beyond the standard model". In: *Nature Reviews Physics* 6.5 (Mar. 2024), pp. 294–309. ISSN: 2522-5820. DOI: 10.1038/s42254-024-00703-6. URL: http://dx.doi.org/10.1038/s42254-024-00703-6.

[10] T. Aaltonen et al. "High-precision measurement of the W boson mass with the CDF II detector". In: *Science* 376.6589 (Apr. 2022), pp. 170–176. DOI: 10.1126/science.abk1781. URL: https://doi.org/10.1126/science.abk1781.

[11] M. Benedikt et al. "Future Circular Colliders succeeding the LHC". In: *Nature Physics* 16.4 (Apr. 2020), pp. 402–407. DOI: 10.1038/s41567-020-0856-2. URL: https://www.nature.com/articles/s41567-020-0856-2#citeas.

[12] *Accelerators — CERN*. May 2025. URL: https://home.cern/science/accelerators.

[13] *High-Luminosity LHC*. May 2025. URL: https://home.cern/science/accelerators/high-luminosity-lhc.

[14] The European Strategy Group. *Deliberation document on the 2020 Update of the European Strategy for Particle Physics*. Tech. rep. Geneva, 2020. DOI: 10.17181/ESU2020Deliberation. URL: https://cds.cern.ch/record/2720131.

[15] O. Brunner et al. *The CLIC project*. 2022. arXiv: 2203.09186 [physics.acc-ph]. URL: https://arxiv.org/abs/2203.09186.

[16] I. Agapov et al. *Future Circular Lepton Collider FCC-ee: Overview and Status*. 2022. arXiv: 2203.08310 [physics.acc-ph]. URL: https://arxiv.org/abs/2203.08310.

[17] The CEPC Study Group. *CEPC Technical Design Report – Accelerator (v2)*. 2024. arXiv: 2312.14363 [physics.acc-ph]. URL: https://arxiv.org/abs/2312.14363.

[18] A. Aryshev et al. *The International Linear Collider: Report to Snowmass 2021*. 2023. arXiv: 2203.07622 [physics.acc-ph]. URL: https://arxiv.org/abs/2203.07622.

[19] E. Sicking and R. Ström. "From precision physics to the energy frontier with the Compact Linear Collider". In: *Nature Physics* 16.4 (Apr. 2020), pp. 386–392. DOI: 10.1038/s41567-020-0834-8. URL: https://www.nature.com/articles/s41567-020-0834-8.

[20] G. F. Knoll. *Radiation Detection and Measurement, 3rd ed.* 3rd edition. New York: John Wiley and Sons, 2000. ISBN: 978-0-471-07338-3, 978-0-471-07338-3.

[21] ECFA Detector RD Roadmap Process Group. *The 2021 ECFA detector research and development roadmap*. Tech. rep. Geneva, 2020. DOI: 10.17181/CERN.XDPL.W2EX. URL: https://cds.cern.ch/record/2784893.

[22] "Physics and Detectors at CLIC: CLIC Conceptual Design Report". In: (Feb. 2012). Ed. by Lucie Linssen et al. DOI: 10.5170/CERN-2012-003. arXiv: 1202.5940 [physics.ins-det].

[23] D. Dannheim et al. *Progress on detector R&D for CLIC 2019–2025*. Tech. rep. Feb. 2025. URL: https://cds.cern.ch/record/2927639/files/CLICdp-Note-2025-001.pdf.

[24] H. Kolanoski and N. Wermes. *Particle detectors: fundamentals and applications*. Includes unchanged reprints with later publication date. Oxford: Oxford University Press, 2020, xvi, 927 pages : illustrations, diagrams. ISBN: 9780198858362. URL: https://bib-pubdb1.desy.de/record/442052.

[25] S. Navas et al. "Review of Particle Physics". In: *Phys. Rev. D* 110 (3 Aug. 2024), p. 030001. DOI: 10.1103/PhysRevD.110.030001. URL: https://link.aps.org/doi/10.1103/PhysRevD.110.030001.

[26] S. Meroli, D. Passeri, and L. Servoli. "Measurement of charge collection efficiency profiles of CMOS active pixel sensors". In: *Journal of Instrumentation* 7.09 (Sept. 2012), P09011. DOI: 10.1088/1748-0221/7/09/P09011. URL: https://dx.doi.org/10.1088/1748-0221/7/09/P09011.

[27] M. Mager. "ALPIDE, the Monolithic Active Pixel Sensor for the ALICE ITS upgrade". In: *Nuclear Instruments and Methods in Physics Research Section A: Accelerators, Spectrometers, Detectors and Associated Equipment* 824 (2016). Frontier Detectors for Frontier Physics: Proceedings of the 13th Pisa Meeting on Advanced Detectors, pp. 434–438. ISSN: 0168-9002. DOI: https://doi.org/10.1016/j.nima.2015.09.057. URL: https://www.sciencedirect.com/science/article/pii/S0168900215011122.

[28] M. Mager. "ALPIDE, the Monolithic Active Pixel Sensor for the ALICE ITS upgrade". In: *Nuclear Instruments and Methods in Physics Research Section A: Accelerators, Spectrometers, Detectors and Associated Equipment* 824 (2016). Frontier Detectors for Frontier Physics: Proceedings of the 13th Pisa Meeting on Advanced Detectors, pp. 434–438. ISSN: 0168-9002. DOI: https://doi.org/10.1016/j.nima.2015.09.057. URL: https://www.sciencedirect.com/science/article/pii/S0168900215011122.

[29] H. Wennlöf et al. "The Tangerine project: Development of high-resolution 65 nm silicon MAPS". In: *Nuclear Instruments and Methods in Physics Research Section A: Accelerators, Spectrometers, Detectors and Associated Equipment* 1039 (Sept. 2022), p. 167025. ISSN: 0168-9002. DOI: 10.1016/j.nima.2022.167025. URL: http://dx.doi.org/10.1016/j.nima.2022.167025.

[30] G. Aglieri Rinella et al. *Characterisation of analogue Monolithic Active Pixel Sensor test structures implemented in a 65 nm CMOS imaging process*. 2024. arXiv: 2403.08952 [physics.ins-det]. URL: https://arxiv.org/abs/2403.08952.

[31] G. Aglieri Rinella et al. "Digital pixel test structures implemented in a 65 nm CMOS process". In: *Nuclear Instruments and Methods in Physics Research Section A: Accelerators, Spectrometers, Detectors and Associated Equipment* 1056 (Nov. 2023), p. 168589. ISSN: 0168-9002. DOI: 10.1016/j.nima.2023.168589. URL: http://dx.doi.org/10.1016/j.nima.2023.168589.

[32] W. Snoeys et al. "Optimization of a 65 nm CMOS imaging process for monolithic CMOS sensors for high energy physics". In: *PoS* Pixel2022 (2023), p. 083. DOI: 10.22323/1.420.0083.

[33] J. A. Ballin et al. "Monolithic Active Pixel Sensors (MAPS) in a Quadruple Well Technology for Nearly 100% Fill Factor and Full CMOS Pixels". In: *Sensors* 8.9 (2008). PMID: 27873817, pp. 5336–5351. ISSN: 1424-8220. DOI: 10.3390/s8095336. URL: https://www.mdpi.com/1424-8220/8/9/5336.

[34] C. Lemoine et al. *Impact of the circuit layout on the charge collection in a monolithic pixel sensor*. 2025. arXiv: 2503.21853 [physics.ins-det]. URL: https://arxiv.org/abs/2503.21853.

[35] F. Krummenacher. "Pixel detectors with local intelligence: an IC designer point of view". In: *Nuclear Instruments and Methods in Physics Research Section A: Accelerators, Spectrometers, Detectors and Associated Equipment* 305.3 (1991), pp. 527–532. ISSN: 0168-9002. DOI: https://doi.org/10.1016/0168-9002(91)90152-G. URL: https://www.sciencedirect.com/science/article/pii/016890029190152G.

[36] I. Kremastiotis. *H2M reference manual*. Tech. rep. Feb. 2023. URL: https://h2m-chip.docs.cern.ch/.

[37] S. Meroli et al. “A grazing angle technique to measure the charge collection efficiency for CMOS active pixel sensors”. In: *Nucl. Instrum. Meth. A* 650 (2011). Ed. by Roland Horisberger, Danek Kotlinski, and Andrey Starodumov, pp. 230–234. DOI: 10.1016/j.nima.2010.12.122.

[38] G. Kramberger et al. “Investigation of Irradiated Silicon Detectors by Edge-TCT”. In: *IEEE Trans. Nucl. Sci.* 57.4 (2010), pp. 2294–2302. DOI: 10.1109/TNS.2010.2051957.

[39] R. Diener et al. “The DESY II test beam facility”. In: *Nuclear Instruments and Methods in Physics Research Section A: Accelerators, Spectrometers, Detectors and Associated Equipment* 922 (Apr. 2019), pp. 265–286. ISSN: 0168-9002. DOI: 10.1016/j.nima.2018.11.133. URL: http://dx.doi.org/10.1016/j.nima.2018.11.133.

[40] *PETRA III - Deutsches Elektronen-Synchrotron DESY*. URL: https://www.desy.de/research/facilities__projects/petra_iii/index_eng.html.

[41] Y. Liu et al. “ADENIUM — A demonstrator for a next-generation beam telescope at DESY”. In: *Journal of Instrumentation* 18.06 (June 2023), P06025. ISSN: 1748-0221. DOI: 10.1088/1748-0221/18/06/p06025. URL: http://dx.doi.org/10.1088/1748-0221/18/06/P06025.

[42] P. Baesso, D. Cussans, and J. Goldstein. “The AIDA-2020 TLU: a flexible trigger logic unit for test beam facilities”. In: *Journal of Instrumentation* 14.09 (Sept. 2019), P09019–P09019. ISSN: 1748-0221. DOI: 10.1088/1748-0221/14/09/p09019. URL: http://dx.doi.org/10.1088/1748-0221/14/09/P09019.

[43] L. Huth et al. *TelePix2: Full scale fast region of interest trigger and timing for the EUDET-style telescopes at the DESY II Test Beam Facility*. 2025. arXiv: 2503.08177 [hep-ex]. URL: https://arxiv.org/abs/2503.08177.

[44] Y. Otarid et al. *Caribou – A versatile data acquisition system for silicon pixel detector prototyping*. 2025. arXiv: 2502.03903 [physics.ins-det]. URL: https://arxiv.org/abs/2502.03903.

[45] Y. Liu et al. “EUDAQ2—A flexible data acquisition software framework for common test beams”. In: *Journal of Instrumentation* 14.10 (Oct. 2019), P10033–P10033. ISSN: 1748-0221. DOI: 10.1088/1748-0221/14/10/p10033. URL: http://dx.doi.org/10.1088/1748-0221/14/10/P10033.

[46] Corryvreckan Authors. *Corryvreckan*. 2021. URL: https://project-corryvreckan.web.cern.ch/project-corryvreckan/.

[47] D. Dannheim et al. “Corryvreckan: a modular 4D track reconstruction and analysis software for test beam data”. In: *Journal of Instrumentation* 16.03 (Mar. 2021), P03008. ISSN: 1748-0221. DOI: 10.1088/1748-0221/16/03/p03008. URL: http://dx.doi.org/10.1088/1748-0221/16/03/P03008.

[48] *Corryvreckan / Corryvreckan · GitLab*. URL: https://gitlab.cern.ch/corryvreckan/corryvreckan.

[49] G. Cowan. *Statistical data analysis*. Oxford University Press, USA, 1998.

[50] J. W. Mayer. "Performance of Germanium and Silicon Surface Barrier Diodes as Alpha-Particle Spectrometers". In: *Journal of Applied Physics* 30.12 (Dec. 1959), pp. 1937–1944. ISSN: 0021-8979. DOI: 10.1063/1.1735093. eprint: https://pubs.aip.org/aip/jap/article-pdf/30/12/1937/18320678/1937_1_online.pdf. URL: https://doi.org/10.1063/1.1735093.